Enhanced recyclability of waste plastics for waterproof cementitious composites with polymer-nanosilica hybrids

Journal Article

Author(s):
Al-Mansour, Ahmed; Yang, Rijiao; Xu, Chengji; Dai, Yuqing; Peng, Yu; Wang, Jiyang; Lv, Qing; Li, Le; Zhou, Chunsheng; Zhang, Zhidong (ID); Zeng, Qiang; Xu, Shilang
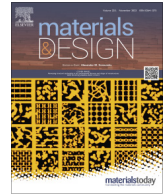
Enhanced recyclability of waste plastics for waterproof cementitious composites with polymer-nanosilica hybrids

Ahmed Al-Mansour [a], Rijiao Yang [a], Chengji Xu [a], Yuqing Dai [a], Yu Peng [a], Jiyang Wang [a], Qing Lv [a], Le Li [b], Chunsheng Zhou [c], Zhidong Zhang [d], Qiang Zeng [a,*], Shilang Xu [a]

[a] College of Civil Engineering and Architecture, Zhejiang University, Hangzhou 310058, PR China
[b] Department of Civil Engineering, Tsinghua University, Beijing 100084, PR China
[c] Key Lab of Structures Dynamic Behavior and Control of the Ministry of Education, Harbin Institute of Technology, Harbin 150090, PR China
[d] Institute for Building Materials, ETH Zurich, 8093 Zurich, Switzerland

HIGHLIGHTS

- EVA-nS hybrids enable recyclability enhancement of waste plastics in cementitious composites;
- The improved plastic-cement interactions promote the engineering properties of cementitious materials;
- XCT with CsI contrast enhancement visualized the superior waterproof performance of the polymer-engineered composites;
- The mechanism of polymerization and nanofilling jointly affect the microstructure and strength of the proposed composites.

GRAPHICAL ABSTRACT
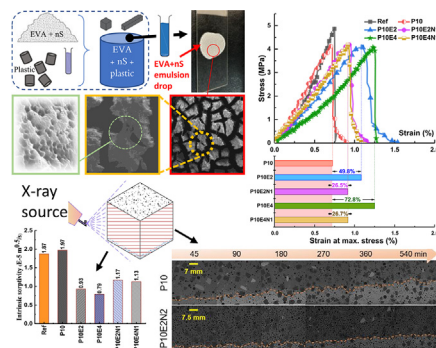
ABSTRACT

Waste plastics may be an environmentally friendly alternative to natural aggregates for concrete manufacture. However, the inferior bond strength between waste plastic aggregates and cement matrix greatly limits the uses of waste plastics for engineering designs and applications. Herein, ethylene–vinyl acetate (EVA) and nanosilica (nS) were jointly employed to enhance the matrix-aggregate interactions in cementitious composites with recycled waste plastics (RWPs). Waterproof properties of the cementitious composites with EVA and nS hybrids were measured. A non-destructive test using micro-focus X-ray computed tomography (μ-XCT) with contrast enhancing technique followed by microstructural tests (SEM/BSE and EDS) were conducted to in-situ trace liquid migration in the composite specimens. The single addition of EVA into the cementitious composites increased the porosity and depressed the compressive strength, but greatly decreased the water sorptivity by nearly 50 %. The organic–inorganic (EVA-nS) hybrids enhanced the recycling potential of the waste plastics in terms of the mitigated strength reduction and improved waterproofing performance. The coupled polymerization of EVA and nanofilling of nS effects were resolved to account for the recyclability improvement. The findings would shed light on design and fabrication of cementitious materials towards large scale recycling methods and technologies of waste plastics.

* Corresponding author.
  E-mail address: cengq14@zju.edu.cn (Q. Zeng).

1. Introduction

Within the construction industry, concrete is well-known as the most consumed material causing huge environmental impacts [1], particularly CO_2 emissions. Aggregates occupy two-thirds of the total volume of a typical concrete. This massive production of these components is accompanied by huge energy consumption and progressive environmental consequences on water, land, and air. In order to limit the negative environmental impacts of the construction sector, which is expected to grow significantly over the upcoming few years [2], various actions have been made. Institutions and foundations have been funding researches on increasing the service life of products/materials and/or closed-loop recycling systems of waste products, especially those with enormous amounts [3,4], such as concrete, metal, plastic, to mention a few.

Generally, the amount of generated waste products are several times more than that being recycled [5], specifically for single-use and rapid disposable materials such as plastics [6,7]. Due to the long-lasting biodegradability of plastics and relatively stabilized characteristics, their aptitude of being recycled in composite materials is high [8], such as concrete. Partial or even full replacement of aggregate with recycled materials shows high potentials to lessen energy consumption and reduce the amount of waste. Due to the high annual production of recycled waste plastics (RWPs) that sets around 120 kg/capita, they have high susceptibility to fit this approach [9]. Although plastic can reduce fire rating of concrete due to its low melting temperature [10–13], it offers preferable characteristics as a concrete component, such as great durability, large flexibility, and high availability [14–16]. In addition to reducing wastes and saving energy and lands, the use of plastic as aggregates reduces the overall construction cost owing to its lightweight compared with typical natural aggregates [17–19].

However, the partial or full replacement of natural aggregates with RWPs has revealed increasing strength reductions as the replacement ratio increased [7,20–22]. Several treatments have been applied to address the strength reduction of concrete with RWP aggregate. For example, sodium hydroxide and sodium hypochlorite, as strong alkalis, were used to modify surface properties of waste plastics, which resulted in better physical and mechanical properties [23]. An improved concrete casting process with ethylene–vinyl acetate copolymer (EVA) enhanced the compatibility between RWP aggregate and cement matrix [21]. In view of the increasing trend of sorptivity in concrete with increasing RWP content [24], nanofillers have been introduced and suggested to enable better waterproof specimens [25,26], particularly to densify the interfacial transition zones (ITZs) between aggregates and the cement matrix.

Likewise, cement has been substituted with other materials to gain improved characteristics in terms of strength, toughness, adhesion, and impermeability [27–32]. One of the widely used organic materials for tuning the microstructure and performance of cement-based materials (CBMs) is EVA [33,34]. EVA is a copolymer of vinyl acetate and ethylene, where the latter is the dominant component. Meanwhile, nano materials (e.g. nanosilica, nS) have been extensively used to improve compactness, strengths, and resistance against water and gas permeability of CBMs [35]. The potential for further applications of EVA and nS, owing to their preferable properties, with RWP cementitious composites may lead to promising results for strengths and waterproofing performance.

Degradation of CBMs is highly dependent on transport characteristics of liquids through their porous media. Practically, a wide variety of CBM structures are rarely in saturated state, and the in-situ water migration may facilitate the penetration of aggressive species (e.g. sulfates, chlorines, carbonates, etc.) that physiochem-

ically and mechanically damage and entangle the durability of such structures [36–38]. The absorption of water by capillary action is known as sorptivity, which may have been firstly used and measured for soils and rocks [39]. It semi-quantitatively assesses the evolution of progressive penetration of liquids into a CBM specimen, which is intrinsically associated with the pore structure of the tested sample [40–43]. Therefore, the comprehensive understanding of capillary sorption in building materials is crucial to accurately evaluate and improve structures' durability during their service life.

Several techniques are available to measure water sorption kinetics in CBMs, one of which is the commonly used gravimetric method that has been standardized in ASTM C1585 [44] and BS-EN 1357 [45], to name a few. Although this method has been analytically upgraded [46,47], it still does not provide data about movement and distribution of liquids inside the tested material [48]. In this method, specimens are oven dried and dipped in water to measure the mass gain over a period of time. This technique has been adopted in a wide variety of sorptivity investigations for air entraining agent concrete [49], self-consolidating concrete [40,50], steam-cured concrete [51], concrete with micro- and macro-silica [52,53], mortars with waste powder of fly ash and marble [54], fiber-reinforced concrete [42], and alkali-activated composites [55–57].

The fundamental analytical approach for the capillary sorption in porous media follows Darcy's law, which enables establishing links between the rate of flow in a material and its hydraulic gradient [58]. A more general term of Darcy's law is the well-known Richards equation [59], that intrinsically takes hydraulic conductivity of a porous material as a function of the moisture content. However, the complexity of liquid migration in CBMs is referred to several pore structural factors, including size, distribution, shape, tortuosity, and continuity of pores [60–62]. Analytical researches have also proposed several factors and modifications to Darcy's law attempting to fit experimental results of different CBMs with analytical approaches [40,47,63].

Non-destructive detecting methods of water penetration and distribution in CBMs have been greatly advanced to deepen the understanding of capillary sorption and waterproofing performance [64,65]. Water ingress in CBMs was successfully visualized in 3D for cracked and uncracked specimens using a technique known as electrical capacitance volume tomography (ECVT) [66]. While documents on Gamma ray (γ) attenuation suggested that results would be more accurate for porous materials with densities much higher than that of a typical concrete [67,68]. Moreover, the use of nuclear magnetic resonance (NMR) revealed varying remarks depending upon the magnetic resonance imaging (MRI) instrument and specimens. NMR has the advantage of visualizing dynamic 2D and 3D distribution and penetration of liquids in non-metallic materials serving a wide variety of applications [69,70], but it could be time demanding and highly sensitive to polymer-based or organic materials [71,72]. Neutron imaging is a powerful measuring technique that relies on the transmitted intensity of neutron beams through a 2D or 3D object [73]. Neutron beams are attenuated based on the chemical composition of nucleus and specimens' geometry [72,74], and they strongly interact with hydrogen nuclei, enabling the observation of water in samples at high spatial resolutions. However, due to the rare availability of neutron beam facilities and expensive resources [73,75], the applicability of the neutron imaging technique is limited.

Micro-focus X-ray computed tomography (μ-XCT) has shown rapid development and wide applications in material science owing to its ease of sample preparation [33,76] and relatively high availability in research laboratories [71]. Nevertheless, a common observation disadvantage of water sorption by μ-XCT is the low

X-ray attenuation of water, which makes it troublesome to be detected by the X-ray imaging technique [77–79]. A comparison study showed that μ-XCT without contrast agent is less efficient to visualize water in porous materials than other more sophisticated imaging techniques (e.g. neutron radiography [80]). Therefore, several studies have used different contrast agents to enhance the visualization of water in μ-XCT images, such as, cesium (Cs) [33,77,78,81–83] and iodide (I) [84–87] solutions. For instance, when a small amount of soluble cesium-based salt (e.g. cesium chloride) was mixed with water for capillary penetration test, the generated μ-XCT images were able to demonstrate water imbibition fronts and paths at high contrast [33,78,82,83]. Such effortless addition could facilitate studies of permeability of porous materials with X-ray imaging techniques.

In this work, a novel mixing method using EVA and nS was developed to enhance the recyclability of RWP in cementitious materials by consolidating compatibility with the cement matrix. Compressive and flexural strengths were provided to show the impact of EVA and nS on the mechanical properties of the cementitious composites. Water uptake in the nano-engineered cementitious composites blended with RWPs were visually evaluated by μ-XCT with the X-ray contrast enhancement agent of cesium iodide (CsI) solution (25 wt%). In addition, capillary absorption tests were conducted following the general steps provided by ASTM C1585 using the CsI solution. Microstructure of the RWP composites were characterized using scanning electron microscopy (SEM) with backscattered electron image (BSE) analysis and energy-dispersive X-ray spectroscopy (EDS). In depth, waterproof mechanisms of the EVA-nS hybrids were explained and schematically visualized inspired by the microstructural images. This work provides a novel technique to enhance the interactions between cement matrix and plastic aggregates, raising the recycling potential of plastic waste for construction materials manufacturing.

2. Materials and methods

2.1. Materials and specimens

The cement binder used in this work is the Chinese PI 42.5 Portland cement, which is identical to ASTM type 1. The chemical compositions of this type of cement and the clinker minerals as received, determined by XRF and XRD tests, are presented in Table 1. The specific surface area of the cement was 355 m²/kg, while the standard consistency was 24.8 %.

A commercially-available quartz sand that meets the Chinese standards GSB 08–1337-2018 was used as the fine aggregate. The particle size distribution (PSD) of the sand was analyzed (Fig. 1), where the largest sand particle did not exceed 4 mm. The natural quartz sands had a SiO_2 content > 96 % and fineness modulus of 2.3 – 2.8 (Xiamen ISO Standard Sand Co., Ltd., Fujian, China), meet-
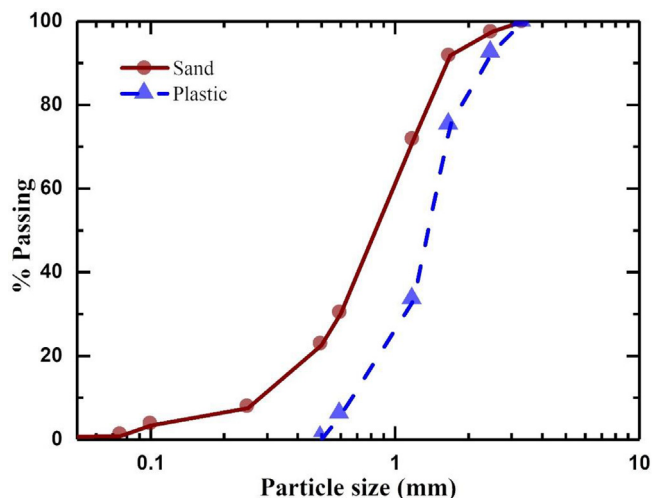

Fig. 1. Sieve analysis of quartz sand and recycled PP.

ing the specified standard. A polypropylene (PP) type RWP was purchased from Xiamen Keyuan Plastic Co., Ltd. The recycled plastics may be originated from packaging, sport equipment, furnishings, food and water containers, etc. The PP possessed density around 1.13 g/cm³ (ASTM D792), and tensile and flexural strengths of 45 MPa (ASTM D638) and 58 MPa (ASTM D790), respectively. The PSD of the recycled PP showed narrower range than the sand used, with an average particle size of 2.18 mm (Fig. 1).

A redispersible EVA with an average size of 571 ± 29 nm was used to tune the compatibility between the RWP aggregate and matrix [21]. The polymerized particles of EVA have shown substantial ability to increases adhesion, deformability, and crack resistance when used in applications with multi-layer films or coatings (e.g. tiles and finishing materials) [88,89]. On the other hand, a type of nS with an average particle size of 91 ± 8 nm was employed to enhance the material microstructure. Owing to the high pozzolanic activity of nS, concrete mixtures with nS exhibited refined pore structures and densified interfacial transition zones [90,91]. This has resulted in improvement in impermeability and chloride attack resistance [92]. Table 2 presents the main physical and chemical properties of EVA and nS. Because polyvinyl alcohol, a protective colloid in EVA, forms crosslinks in an alkaline solution, sodium hydroxide solution of 2 wt% was prepared to guarantee better dispersion of both additives.

PSDs of both EVA and nS powders were obtained by NANO-SIGHT NS500 machine (Malvern Instruments Ltd). Preparations of emulsions started by mechanically mixing powders with water at a ratio of 1:9 for 10 min at a stirring speed of 400 rpm. The suspension or emulsion was diluted to conform the machine detection requirements. 25 frames per second were captured as the suspension flowed in the machine, with 607 slider shutter and 15 slider

Table 1
Chemical compositions of cement and minerals of clinker.

Chemical compositions of cement %		Minerals of clinker %	
Calcium oxide (CaO)	61.02	Tricalcium silicate (C_3S)	59.03
Silica (SiO_2)	20.94	Dicalcium silicate (C_2S)	16.47
Alumina (Al_2O_3)	4.85	Tricalcium aluminate (C_3A)	6.79
Iron oxide (Fe_2O_3)	3.44	Tetracalcium aluminoferrite (C_4AF)	11.73
Magnesium oxide (MgO)	1.70		
Sulfur trioxide (SO_3)	1.88		
Loss on ignition (LOI)	1.88		
f-CaO	0.5		
R_2O	0.5		

Table 2
Main physical and chemical properties of EVA and nS.

EVA		nS	
Density (g/cm³)	1.3 ± 0.02	2.4 ± 0.2	
Mean particle size (nm)	571 ± 29	91 ± 8	
D10 (nm)	110 ± 18	78 ± 10	
D50 (nm)	377 ± 33	181 ± 25	
D90 (nm)	663 ± 80	223 ± 40	
Solid content (%)	99 ± 1	Purity (%)	> 99.9
Protective colloid	Polyvinyl alcohol	Specific surface area (m²/g)	420 ± 30

grains. The distribution curves of EVA and nS particles are demonstrated in Fig. 2. It can be noted that EVA (Fig. 2a) and nS (Fig. 2b) were more than one order and two orders of magnitudes thinner than cement, respectively.

The replacement ratios of EVA and nS to cement were limited to 4 % [93,94] and 1 % [95,96], respectively. Table 3 lists the designed mix proportions (in kg/m^3) and replacement ratios. The nomenclature was made as follows: Px + Ey + Nz, where P, E and N represent plastic, EVA, and nS, respectively, and ×, y and z represent their content. It is worth noting that EVA and nS may have significant opposite effects on CBMs' workability, while EVA tends to increase workability [28,88,97], nS decreases it [96,98,99]. Therefore, water contents of mixtures were slightly tuned to keep consistent slump of 115 ± 10 mm. Slump tests were conducted following the guidelines of ASTM C143 [100].

Cubic specimens with a side length of 5 cm were cast. Firstly, water was mixed with 2 wt% sodium hydroxides to prepare a highly alkaline solution; then, EVA was mechanically mixed with the solution for 5 min at 400 rpm. During the mixing, nS was gradually added to the mix to prevent agglomeration. Later, RWPs were added to the solution with continued mixing for another 5 min. Note that because the PSD of the RWP (PP type used) is different from that of sand, the replacement of sand with PP was performed with further sorting of sizes. In other words, RWP particles replaced equivalent sizes of sand particles, and the resulting sand + RWP mix possessed an equivalent PSD to that of the natural quartz sand, which is shown in Fig. 1. After that, the EVA-nS-RWPs mixture was poured into a homogenous cement-sand mixture which had been dry-mixed at 60 rpm for 3 min. With further stirring for 3 min, the cementitious composites slurries were readily prepared and cast in cubic mold in the side length of 50 mm with vibrations for 30 s. Following surface finishing, the top surface of each specimen was covered with a thin layer of plastic film to prevent water evaporation. After a primary curing for 1 day, specimens were demolded and stored in a curing room at a temperature of 22 ± 3 °C and humidity of 98 ± 2 % until testing date.

2.2. EVA/nS emulsion stimulation

The microstructural alterations due to the additions of EVA and nS were discretely detected on a glass surface as shown in Fig. 3. While nS particles agglomerate in sperate units when being in contact with water [91], EVA particles create bubble-like connected films [28]. During mixing, small amount of the EVA/nS emulsions were collected in glass tubes and a drop was dripped on a glass surface (Fig. 3a). Once the drop was air-dried at room temperature, SEM/EDS tests were performed. Fig. 3b shows separate units of agglomerates of nS that are randomly connected by EVA films, as

shown in the higher magnification image in Fig. 3c. The table in the bottom left illustrates the EDS element analysis results for two different spots, R1 and R2 (see Fig. 3c). The detected elements are carbon (C), oxygen (O), and silica (Si). Spot R1 is on a nS unit, showing higher Si and O readings, and of course some amount of C because of the existence of EVA in the emulsion. Spot R2, however, was placed on the connecting films, which primarily shows high values for C verifying the key component of EVA.

2.3. Mechanical tests

Compressive and flexural strengths of each mixture were tested in an INSTRON 8802 full functional servo-hydraulic testing machine. Force control at 30 MPa/min was applied for compression tests, and displacement control at 1 mm/min was applied for flexure tests. For each mixture, three specimens were tested, and the strength values were averaged. RWP aggregates were included in 30 out of 36 cubes and prisms that were totally tested, as shown in Table 3.

To precisely compare the specimens and observe the mechanical changes due to the use of EVA and nS, results of three specimens were averaged for each test. Specimens' sides were carefully checked beforehand, and they were set on the supports of the loading machine horizontally using an alcohol glass tube. Between the prisms and the loading rod, a 5-mm thick leather was placed, and a 0.1-mm thin paper was utilized to avoid unwanted gaps [101]. Before loadings, all stress and strain data in the machine were set to zero, and loading parameters were fixed, so consistent results of each mix can be obtained.

2.4. Waterproof tests

Waterproof property of the RWP cementitious composites was assessed by water imbibition. Cubic specimens at 180 d were adopted for waterproof tests. A thin layer (≤1mm) at the water-contacted face of each specimen was removed using Abrasi-Met 250 cutter to avoid the effects of the oily removing agents used for demolding. The main steps of the sorption test are demonstrated in Fig. 4. Before the tests, samples were completely dried to constant weights. Drying temperature varied in guidelines and published investigations, e.g., 40 °C [57], 44 °C [102], 50 °C [44,84,86], 55 °C [87], 60 °C [51,78,82,83,103], 70 °C [104], 80 °C [40], and 105 °C [47,48,105]. However, it was reported that the drying temperature higher than 50 °C may cause non-negligible damages to the microstructure of CBMs [106,107]. A study evidenced that the possible microstructure changes induced by drying at 50 °C would take limited impacts on the water sorptivity of CBM specimens [108]. Therefore, the temperature of 50 ± 2 °C was set in an oven with air circulation to remove the water confined in the
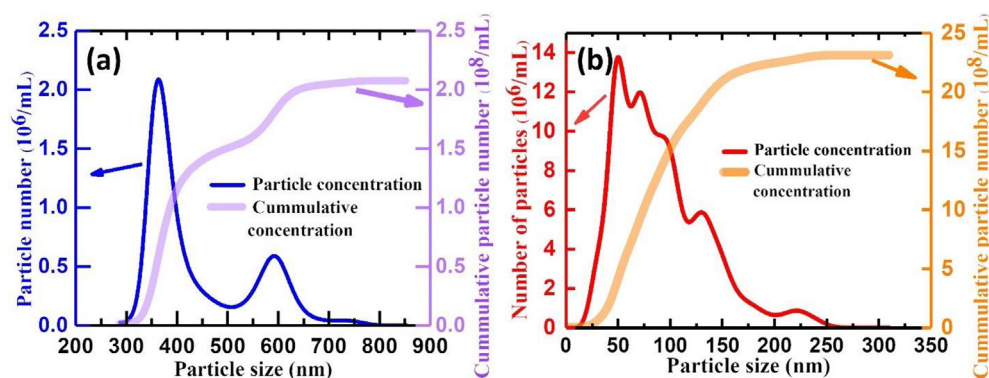

Fig. 2. Particle concentration of (a) EVA and (b) nS.

Table 3
Designed mix proportions.

Mix ID	Cement	Mix proportions in kg/m^3					EVA/cement (%)	nS/cement (%)	Water/cement	Water/solid
		EVA	nS	Sand	Plastic	Water				
Ref	525	0.0	0.0	1495	–	236	0	0	0.450	0.450
P10	525	0.0	0.0	1245	149	236	0	0	0.450	0.450
P10E2	510	10.5	0.0	1245	149	228	2	0	0.447	0.438
P10E2N1*	506	10.5	5.3	1245	149	240	2	1	0.474	0.460
P10E4	497	21.0	0.0	1245	149	226	4	0	0.455	0.436
P10E4N1	489	21.0	5.3	1245	149	235	4	1	0.481	0.456

* P: polypropylene, E: EVA, N: nanosilica.
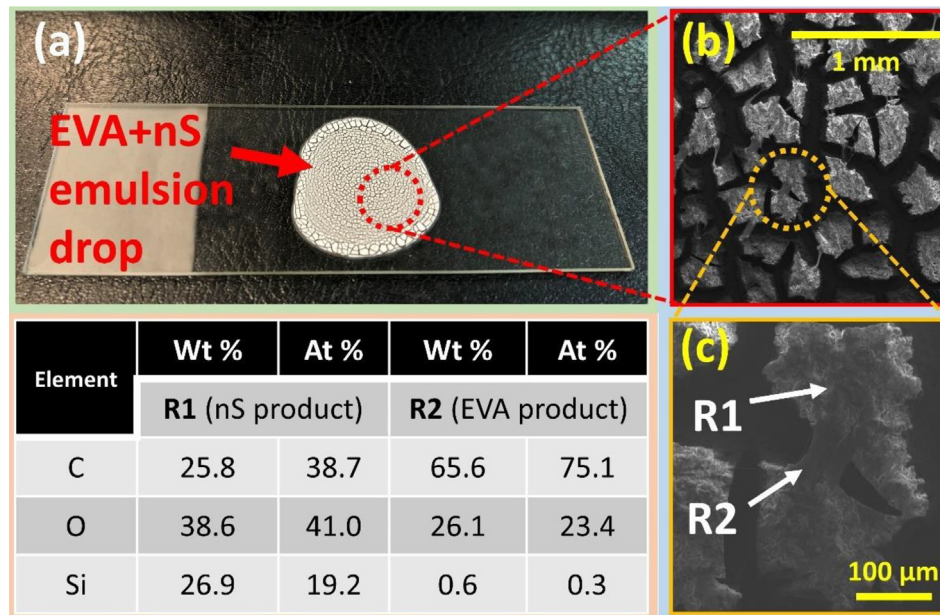
Fig. 3. Preparation process of the EVA + nS emulsion: (a) a drop of the emulsion on a glass surface, (b) SEM micro morphology, and (c) a higher magnification image showing nS agglomerations with connecting EVA films. EDS results of R1 and R2 spots are represented in the bottom left table for carbon (C), oxygen (O), and silica (Si).

specimens, which is also suggested by ASTM C1585 [44]. After the complete drying status of the specimens was reached (the mass changes in 24 h less than 0.1 %), they were left to cool down at room temperature (22 ± 1 °C) (Fig. 4a). To control the direction of solution absorption, four sides of each specimen were coated with epoxy resin, leaving the top and bottom sides free of coatings. After the epoxy coatings hardened at ambient temperature for 24 h, specimens were again oven-dried at 50 °C for 72 h. Then, the specimens were placed by their bottom surface on plastic supports that had been immersed in CsI solution (25 wt%) so that the solution level was 1 to 3 mm above the top of the supports (Fig. 4b). During sorption, the specimens were weighed by an electronic balance with the accuracy of 0.01 g at different time intervals: 0 (before immersion), 45, 90, 180, 270, 360, 540 min.

At set time, excess surface water was removed by a damped paper towel [44]. Within a minute, each sample was weighed and carefully transferred to the μ-XCT machine (Fig. 4c). The device used for the X-ray scans was XTH255/320 LC (Nikon, Japan) with the accelerating voltage of 120 kV and the beam current of 80 μA. A Cu film of 1.5 mm was attached on the X-ray emitter to reduce beam hardening artefacts in the X-ray tomograms. A detector with the resolution of 2000 × 2000 pixels was attached on the backboard of the testing chamber to collect the transmitted X-ray beams. Each specimen was fixed on the sample stage between the X-ray emitter and the detector (see Fig. 4c for more details). Here, as each cubic specimen rotated by 360°, 2000 high-resolution pro-

jections were acquired from different angles. Each μ-XCT scan lasted for 18 min and generated multiple projections that were reconstructed using CTPro software to build a wide-range gray level 3D model for each specimen. Using the tomographic lensfree sensor with the above parameters, the spatial resolution created an effective voxel size of 0.041 μm for the total volume of each specimen in X, Y, and Z directions. Finally, the 3D models were imported to a microstructure analysis software (VG Studio 3.1) to process phase segmentation and visualization based on their X-ray attenuation coefficients.

The mass gain of each specimen at different time intervals was used to evaluate the so-called mass transport [46,109,110] or mass sorptivity [33]. Because mass gain was immediately followed by m-XCT, which required special preparation of samples and testing tools, each one of the three cubes of every mixture was used twice (45 and 270, 90 and 360, 180 and 540 min). Those cubes were cast from the same mix and at the same time. Side length, density, and porosity of specimens of the same mix were checked beforehand to guarantee the data consistency. Mass gain ($\Delta\omega$) was calculated by subtracting the pre-dried mass (ω_o) from the total mass at each time interval (ω_t) using Eq. (1), where all variables are in g.

$$\Delta\omega = \omega_t - \omega_o \qquad (1)$$

The mass sorptivity (S_m) was evaluated using the mass absorbed ($\Delta\omega$) and time (t) using Eq. (2) according to the Lucas-Washburn (LW) equation [33]:
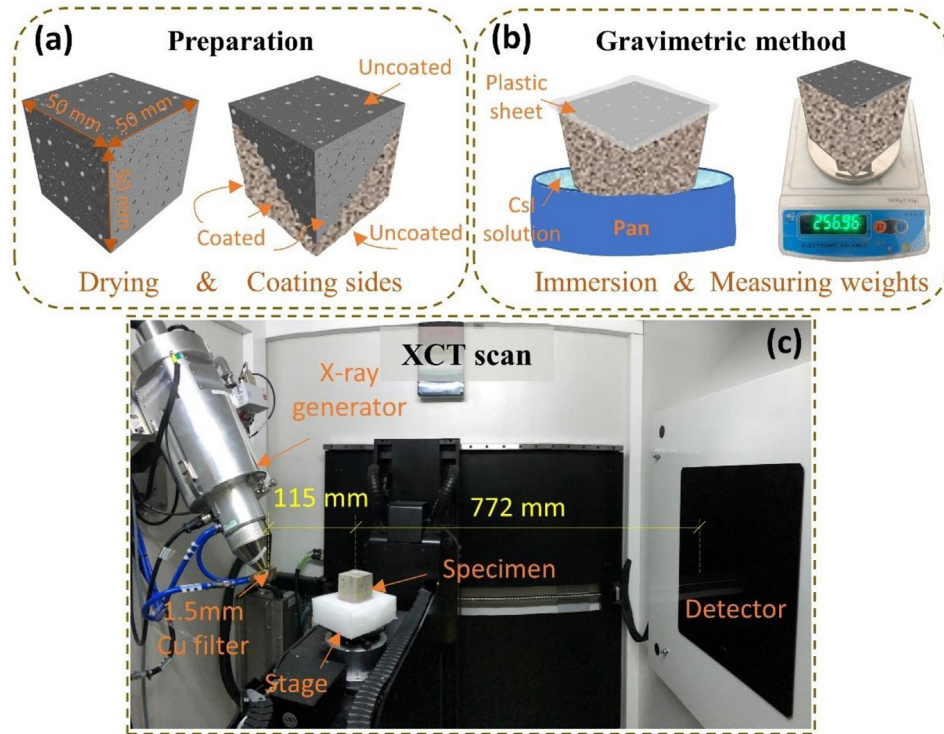
Fig. 4. Schematic illustration of the waterproof test: (a) preparation of specimens: drying and coating, (b) sorptivity test in CsI solution and measuring weights at 0, 45, 90, 180, 270, 360, and 540 min, and (c) μ-XCT scans.

$$\Delta \omega = S_m \sqrt{t} \tag{2}$$

Within the same regime, the sorptivity (S_l) measured by liquid uptake height (ΔL) can be expressed as [111]:

$$\Delta L = S_l \sqrt{t} \tag{3}$$

To take into consideration surface tension (γ) and dynamic viscosity (μ) of the penetrating liquid, intrinsic sorptivity (S_i) can be found using Eq. (4), where (S_l) is taken in m/s$^{0.5}$, γ in N/m, and μ in Pa.s.

$$S_i = \frac{S_l}{\sqrt{\gamma/\mu}} \tag{4}$$

For porous material with homogenous pore structure, mass sorptivity (S_m) can be translated to depth sorptivity (S_l) when taking into account porosity (φ) and sorption area (A) of the specimens and density of the penetrated liquid (ρ_l):

$$S_m = \rho_l A \varphi S_l \tag{5}$$

Using Eqs. (4) and (5), the intrinsic sorptivity (S_i) by mass can be found as follows [33,112]:

$$S_i = \frac{S_m}{\rho_l A \varphi \sqrt{\gamma/\mu}} \tag{6}$$

2.5. SEM/EDS scans

To observe the microstructure of the cementitious composites and detect the possible alterations due to the migration of CsI solution, the modes of secondary electron (SE) and backscattered electron (BSE) in SEM were used. Moreover, energy-dispersive X-ray spectroscopy (EDS) test was conducted to enable chemical characterization. This allowed us to explore the liquid transport paths by tracing Cs and I. A FEI QUANTA 650 FEG device was used with a voltage of 20 kV and a spot size of 4 nm.

Once the sorptivity test to evaluate waterproof of specimens was finished, small segments at the sorption heights were acquired to prepare the samples for SEM tests. Then, the segments were oven-dried at 50 °C for 24 h. For ordinary SEM tests, a platinum coating was performed to make the tested surfaces electrically conductive, which as a result produced clear and high-quality images. For BSE tests, samples were impregnated in epoxy resin and then polished to get horizontal and smooth surfaces. The polishing scheme with SiC papers of 400, 800, 1200, 2000, and 4000 grits, each of 2 min, was adopted to control surface roughness of the samples. After drying and coating, the samples were readily prepared for BSE tests.

3. Results and discussions

3.1. Mechanical properties

Load-displacement curves of specimens at 28 d for compression and flexure tests are shown in Fig. 5. Generally, the partial replacement of natural sand with PP was accompanied by reductions in both strengths [1,17,21,25,26]. More importantly, the addition of small portions of EVA brought positive changes to the strain patterns. For compressive stresses, Fig. 5a shows that the Ref specimen performed linearly within the elastic deformation range, reaching a maximum-stress strain of 2.2 %, which was the least among all other specimens. Other specimens, particularly with EVA, performed differently, showing substantial decreases in the stress–strain slopes and reaching higher strains within the elastic region. This pseudo-ductile performance is clearly observed particularly in the EVA-nS-modified RWP composites, which could be suitable for many civil engineering applications [113]. The reason behind this behavior is the elastic nature of the polymeric films that EVA creates when reacting with water [88,94] (see also Fig. 3), and probably the more porous microstructure of specimens
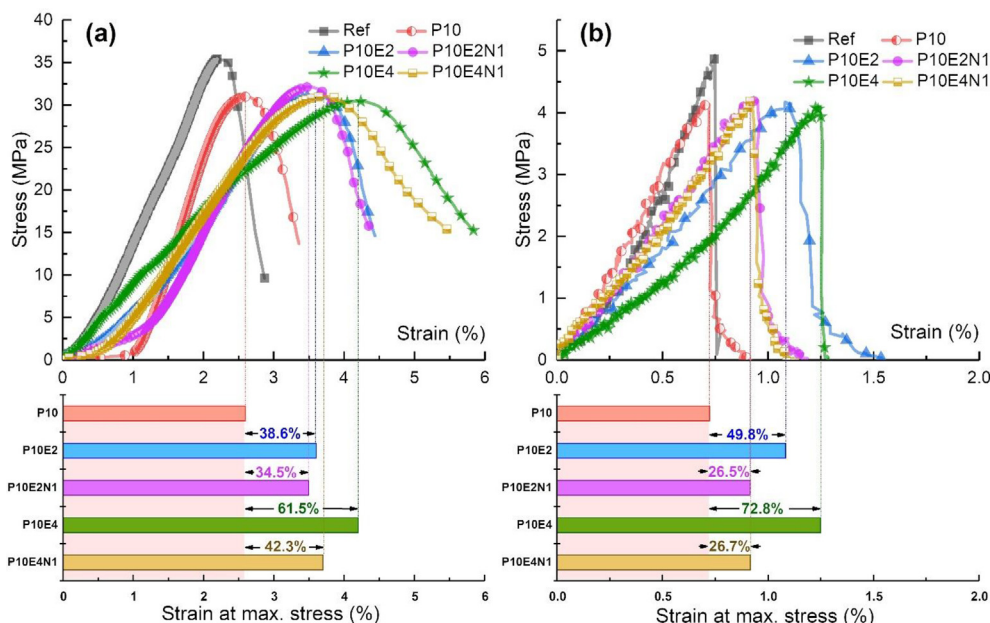
Fig. 5. Load-displacement curves of specimens at 28 d and the corresponding peak-fore deformations with comparisons: (a) compression and (b) flexure tests.

with EVA (discussed in Section 3.2) that produces more voids for the cement matrix particles to move in.

The relative changes of the strains at maximum compressive stresses of specimens are shown in the lower part of Fig. 5a. The increasing strain pattern is clear in the EVA-engineered specimens. The relative increase of P10E2, compared with P10, was around 38.6 %, which then raised to 61.5 % when 4 wt% of EVA was added. Likewise, flexural behavior of specimens with EVA had more pseudo-ductile performance than Ref and P10, see Fig. 5b. Compared with P10, P10E2 and P10E4 performed considerably well with 49.8 % and 72.8 % more peak-stress strains than P10, respectively. It is noteworthy that the addition of nS to some extent increased maximum allowable stresses (as discussed in the following paragraph), but also slightly decreased peak- stress strains compared with specimens with EVA only. From a structural point of view, those higher elastic strains of the polymer-modified specimens are translated into higher energy absorption before total failure [21,88], which would increase the scope of applications in practice.

Fig. 6 shows the compressive and flexural maximum stresses of specimens at 28 d. Regardless of the additions of EVA and nS, the cementitious composites with RWP had an average of 12.2 % less compressive strengths and 15.7 % less flexural strengths compared with the Ref specimen. This reduction is attributed to the weak body of plastic aggregates [19,26], which possess higher deformability than natural sand. When mechanical tests are carried out on cement-based specimens, components suffer high shear and bearing stresses. Plastic aggregates reach their maximum allowable stresses first due to their weak body and plastic behavior [114], which also explain the higher strain at maximum stresses compared with the Ref specimen (Fig. 5a). Note that the increased pore volume of matrices with RWP could also reduce the overall mechanical performances [17,21,115], resulting in poorer bonding between RWPs and the cement matrix. The pore volumes of matrices were observed by μ-XCT and discussed in the following section. The addition of EVA and nS, however, mitigated strength reductions and showed promising results.

RWP cementitious composites with EVA-nS hybrids showed increased compressive strength (Fig. 6). The cementitious composites with 2 % EVA witnessed slight increases in compressive
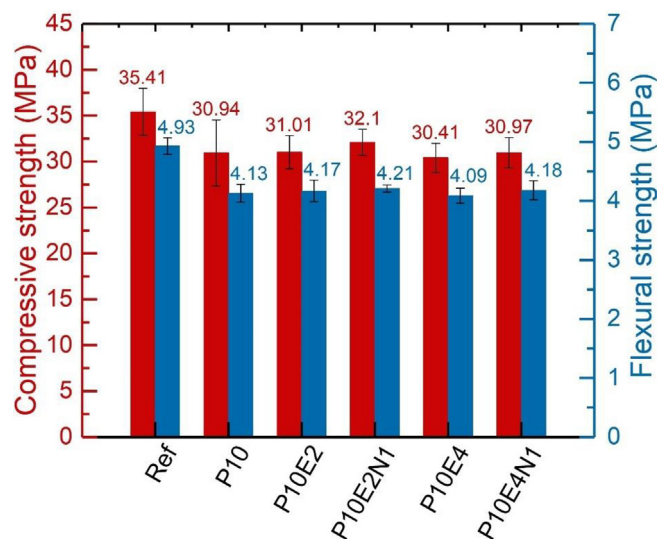

Fig. 6. Mechanical properties of specimens at 28 d: compressive and flexural strengths.

strengths owing to the transition zone effect that EVA created between RWP and cement matrices [21]. An obvious increase of nearly 4 % was observed for P10E2N1, which was believed to be from the densification of microstructures by nS [90,116]. The further increase of EVA to 4 % in mixtures with RWP produced more porous structures, which resulted in inferior compressive strengths. Compared with P10, P10E4 had about 1.8 % less compressive strength. The addition of nS to the latter mixture densified the microstructure, but the improvement was negligible. The undesirable effect of EVA on compressive strength of mixtures has been refereed to its interconnected layers that builds when mixed with water, which blocks and affects the growth of hydration products [29,52].

On the other hand, the figure shows slightly different effects of EVA and nS on the flexural behavior of RWP cementitious composites. The effect of EVA (even at higher dosage, 4 %) did not cause

perceptive damage, nevertheless, the further addition of nS enhanced the strength-decrease mitigation effect significantly. For instance, when 2 % of EVA were added, flexural strength of P10E2 was just above 1 % higher than that of P10. The microstructural alterations of EVA seemed to bring different effects for flexural strength than it did for compressive strength, which has been reported elsewhere [29,117,118]. Although nS could improve flexural strength by densifying cement matrices [99], the effect of high amount of EVA to reduce strengths prevailed (P10E4). The reason for this is that high volumes of EVA created thicker foam-like microstructure that would enable higher deformability but less rigidity [119].

3.2. Pore structure of specimens

Porosity was investigated by μ-XCT. Here, a size of 64,000 mm^3 was selected as the region of interest (ROI) for all specimens. 2D and 3D images and values of porosity of each mixture are shown in Fig. 7. Each 2D μ-XCT image shows five different phases: a) dark circles that represent isolated pores in the cement matrices with the lowest X-ray attenuation; b) dark gray polygons that represent the plastic aggregates, which cannot be seen in the Ref specimen because it does not have plastic aggregates; c) gray phase that integrally comprises different cement hydrates with indistinguishable gray values; d) large sand particles shown in relatively bright polygons; and e) small bright dots that represent the unhydrated cement particles. It is worth noting that the unhydrated cement particles are tiny and minimal, because all specimens were tested at the age of 180 d.

For 3D μ-XCT demonstrations, the solid phases of one half of each 3D image were set as transparent, so the pores can be clearly illustrated with different colors according to their volumes (Fig. 7). Indeed, the porosity was significantly increased when adding EVA to the cementitious composites due to its air entraining effect
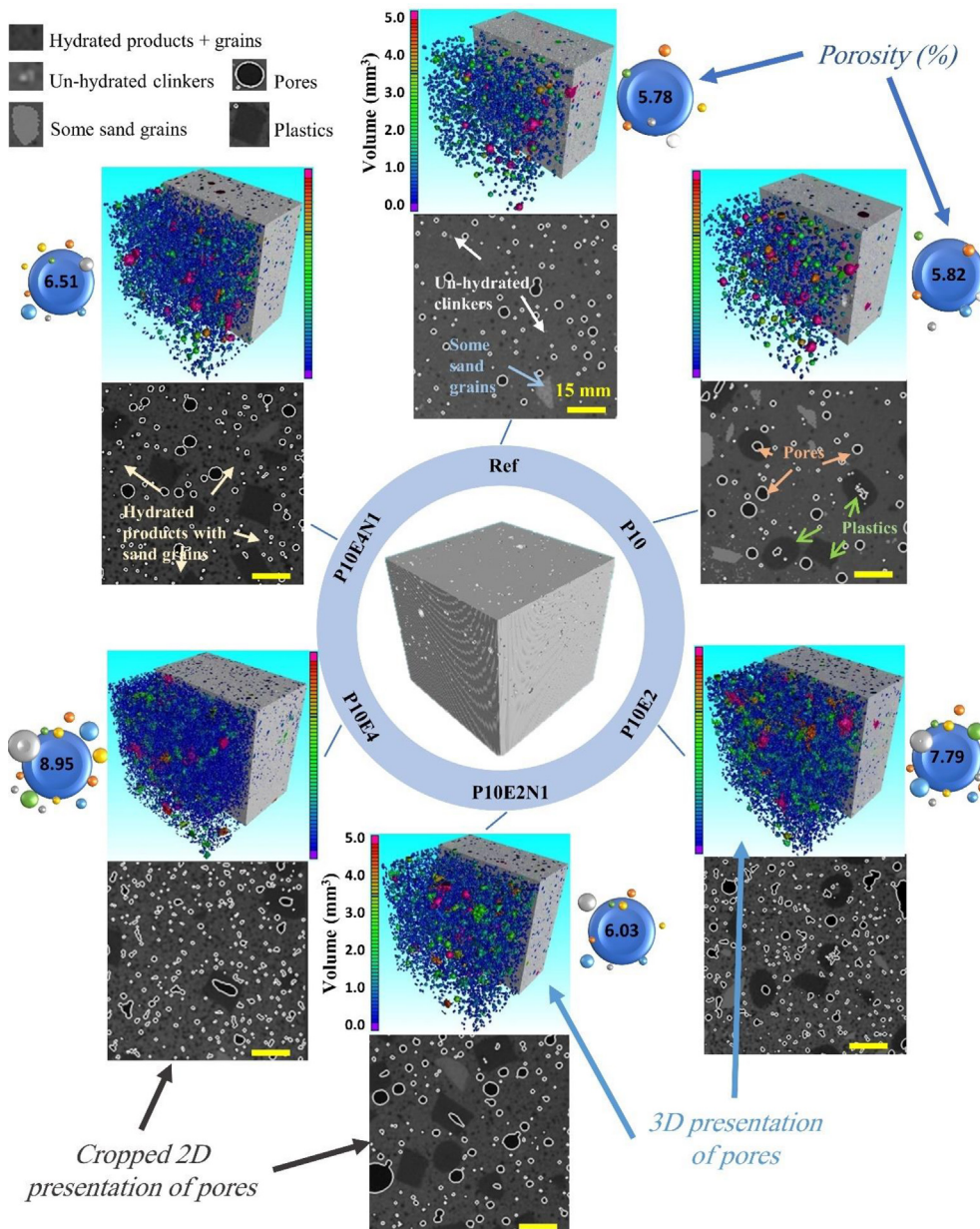

Fig. 7. 2D and 3D μ-XCT images of the Ref at the top, and going clockwise for other specimens in order: P10, P10E2, P10E2N1, P10E4, and P10E4N1. Air voids are demonstrated in the 3D μ-XCT images based on their volumes. Porosities are indicated in circles besides each 3D image.

[29,93]. However, the opposite effect on porosity was noted by adding nS, owing to forming more CSH gel and filling the small voids in cement matrices [90,92]. The 3D μ-XCT images enabled the demonstration of the effect of EVA on the polymer-modified mixtures due to the air-entraining effect through increasing air voids whose volumes are much less than 1 mm³. These findings are in line with previous studies [28,33]. The Ref and P10 mixes had porosities around 5.8 %, which then increased to 7.79 and 8.95 % when adding 2 and 4 wt% EVA, respectively. One can observe a reduction of around 25 % in porosities when 1 wt% of nS was added to the EVA-modified cementitious composites. This testified that nS substantially enhanced the compactness of CBMs.

Fig. 8 provides quantitative pore characteristics of the cementitious composites in terms of mean diameter, sphericity, and compactness [120]. Here, mean diameter is the maximum permissible diameter of pores, which is given in mm; sphericity is the ratio between the surface of an ideal sphere (A_{shpere}) with the same volume as a pore and the surface of the same pore (A_{pore}), provided by A_{shpere}/A_{pore}; while compactness is the ratio between the volume of a pore (V_{pore}) and the volume of the corresponding circumscribed ideal sphere (V_{sphere}), given by V_{pore}/V_{sphere}. Both sphericity and compactness range from 0 to 1, with 1 representing a pore with characteristics of a sphere with the same size. Mean size directly reflects the pore size in statistic manner, while mean sphericity and compactness characterize the geometry and shape of the pores [33]. Although EVA increased porosity in the specimens (Fig. 7), it also decreased pore diameter (Fig. 8). This is more likely referred to the polymeric network created by the polymerized EVA particles in cementitious composites. Sphericity did not show significant changes between the mixtures blended with EVA and those with nS, however, compactness decreased as EVA content increased. Due to the different nature of polymers and their interaction mechanisms [89], the effects on the cementitious composites in altering their pore characteristics by EVA are more obvious than nS.

3.3. Waterproof behavior

The resistance of cementitious composites against liquid transport is a major criterion for waterproof property. Typically, mass sorpti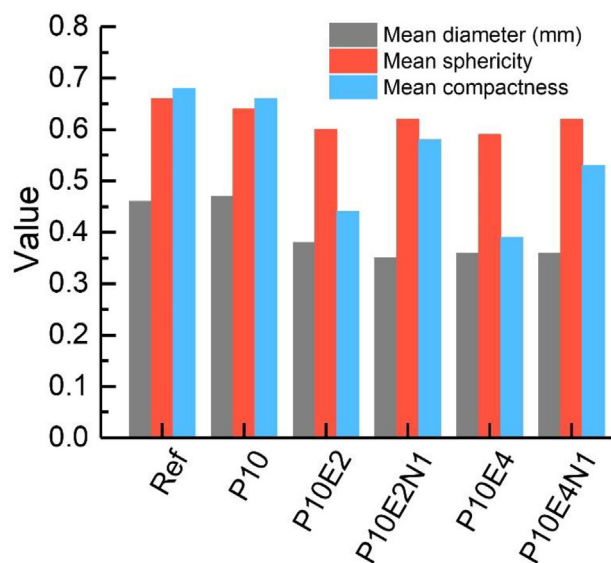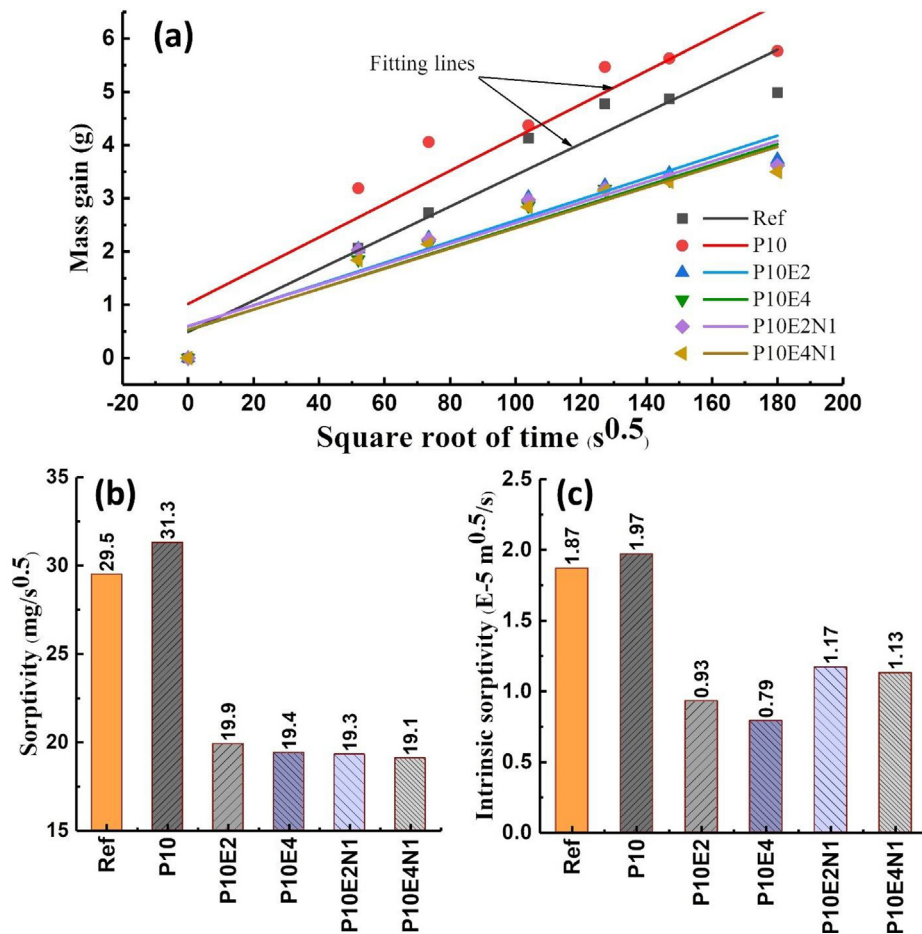vity is an easy approach that provides useful information about liquid transport kinetics. Fig. 9a shows the mass gain in (g) versus the square root of time in (s^0.5) with linear fittings of the specimens. The best linear fitting lines were plotted to obtain the initial sorptivity that relies on the slope of these lines [44]. It is clear that there are two main streams distinguished by the existence of EVA. Generally, mass accumulated over time at the initial mass rise was much faster than the later stages, which may be due to the filling of large capillary pores and/or cavities near the surface at the very first liquid sorption and the interactions between cement hydrates and water molecules [40,121,122]. The reduction rate was more significant in the EVA-modified specimens owing to the spatially-connected polymer films that enhanced the waterproof performance of the porous composites (Fig. 3b and c, see also [33]).

Fig. 9b provides the mass sorptivity for the tested specimens. The direct incorporation of the PP particles in cementitious composites slightly increased the mass sorptivity from 29.5 to 31.3 mg/s^0.5 by 6.01 %. However, when EVA was employed, the mass sorptivity was substantially decreased from around 30 mg/s^0.5 to nearly 19 mg/s^0.5 by at least 35 % (Fig. 9b). While polymer-modified cement materials may own air-entrainment characteristic with higher air voids in the matrix (Fig. 7, see also [123]), the formation of EVA polymer networks can block interconnected open channels for water penetration and consequently decrease the water capillary imbibition in the EVA-modified mortars. To take into account the physical parameters of the CsI solution (i.e. density, surface tension and dynamic viscosity), the intrinsic sorptivity was calculated using Eq. (6) and presented in Fig. 9c. For the CsI of 25 wt%, its density was 1254.4 kg/m³, surface tension was 76.91 mN/m, and dynamic viscosity was 1.01×10^{-3} pa.s, as interpolated from existing values in the literature [124]. These values were unified in Eq. (6) for all mixtures, but the porosity data varied for different specimens. The variations in porosities within the mixtures was due to the use of nS, as the latter produced denser specimens. Estimation showed that the intrinsic water sorptivity was slightly increased by 5 % when PP was directly recycled as the aggregate in P10 mixture (Fig. 9c). The pore obstruction effect of EVA drastically decreased the intrinsic permeability by 53 % for P10E2 and by 60 % for P10E4 compared with P10 (Fig. 9c). Note that when nS was incorporated into the mixture by 1 %, the intrinsic permeability surprisingly increased by 26 % and 43 % compared with the EVA-modified composites without nS. This was because the cementitious composites with nS showed lower porosity, according to Eq. (6), which would yield a lower intrinsic water sorptivity for the materials with similar mass sorptivity.

The benefit of using CsI to trace water uptake in porous cementitious composites becomes obvious when generating and processing μ-XCT data, in which the increased X-ray attenuation provides clear and easily-distinguished images. Fig. 10 shows a representative illustration of processed μ-XCT data for P10E2 after being immersed in CsI solution for 360 min. The invasion process of the CsI solution is shown in orange in the 3D model in Fig. 10a, while the rest of the model is in gray. Some particles with the X-ray attenuation coefficient close to the CsI filling the cement matrix were also shown in orange. Fig. 10b shows a cross section near the top surface that is beyond the water penetration fronts. The attached gray value histogram with four peaks in Fig. 10c enabled the identification of four main phases: pores at a gray value in the range of 31–33; PP particles at a gray value range of 50–52; cement matrix without CsI filling at a gray value in the range of 73–75; and some natural aggregates at a gray value of 96–98 (Fig. 10c).

Fig. 10d displays a cross section near the water penetration front of P10E2. Part of the cement matrix became brighter due to the partial CsI filling, and the intensity of the last peak with the gray values of 96–98 was drastically increased from 1000 to

Fig. 8. Pore characteristics measured by μ-XCT in the specimens: mean diameter (mm), sphericity, and compactness.

Fig. 9. Mass sorptivity results: (a) mass gain of specimens after sorption in CsI solution, (b) mass sorptivity calculated from the slope of the fittings in the mass gain-time$^{0.5}$ relationship, and (c) intrinsic mass sorptivity (Eq. (6)) after taking into account the liquid properties (i.e. density, surface tension, and viscosity).

8500 (Fig. 10e). Otherwise, little changes can be found from the sectional image when compared with Fig. 10b. Finally, Fig. 10f unveils a cross section of P10E2 fully saturated with CsI solution. The cement matrix became brighter, and the pores and plastic aggregates were clearly observed. Analysis on gray value histogram indicated that the last peak was greatly raised to 20000, the third peak (indicating cement hydrates) was substantially decreased, and the first and second peaks had no significant changes (Fig. 10g). The changes in gray value histogram of cementitious composites before and after the sorption of a solution with contrast agent may help better characterize the pores and cement matrix. Indeed, a previous work suggested that the dyeing of cement matrix may separate the cement matrix from aggregates, which would widen the application of XCT [83].

Fig. 11 shows vertical 2D cross-sectional µ-XCT images for specimens with CsI penetration over time. The figure consists of six rows (Ref, P10, P10E2, P10E4, P10E2N1, and P10E4N1) and six columns (45, 90, 180, 270, 360, and 540 min). Each one of the three cubes of each mixture was used twice in this test, and the sectional images were acquired based on the clearness and consistency of the sorption height. Dotted lines were drawn in the XCT images to demonstrate the liquid migration fronts that can lucidly separate the CsI-saturated and unsaturated zones. Clearly, the penetration heights of the Ref and P10 specimens were higher than those of the others, reaching more than half of the total height in 540 min. The EVA-modified cementitious composites showed significant waterproofing performance, limiting the maximum penetration to less than one-third of the total height. This behavior is

referred to the polymeric films that partially block the penetration paths (connected voids) in the microstructure of the cement matrix, resulting in higher waterproofing performance. Further addition of nS into the mixtures with EVA showed minor influences on the water penetration heights (Fig. 11). The results were consistent with those of mass sorptivity (Fig. 9a).

To qualitatively evaluate the capillary penetration rate from the µ-XCT images shown in Fig. 11, the solution rising height of each specimen was measured. Five measurements at different locations were averaged for each image to acquire reliable penetration heights. Fig. 12 shows the solution penetration rates of the specimens (liquid height to total specimen height) after being immersed in CsI solution for 45, 90, 180, 270, 360, and 540 min. For instance, within the first immersion time (45 min), rises of the CsI solution into the Ref and P10 specimens exceeded 10 % of the total height, while those were around 8 % and 6 % in the mixtures with 2 % and 4 % EVA, respectively. It could be concluded that the addition of EVA, even at small portions, could provide easily distinguishable waterproof behavior against water migration compared with other specimens [33,125].

The differences between mixtures with and without EVA were maintained as immersion time increased. Within 45 min, the polymer-modified cementitious composites were nearly 48 % more waterproof than Ref and P10, showing crucial improvements during the first moments when water gets capillary-absorbed into the specimens. The relative changes of the liquid uptake height slightly decreased in 90 min when more water particles filled the large and near-surface pores and migration paths in the specimens.
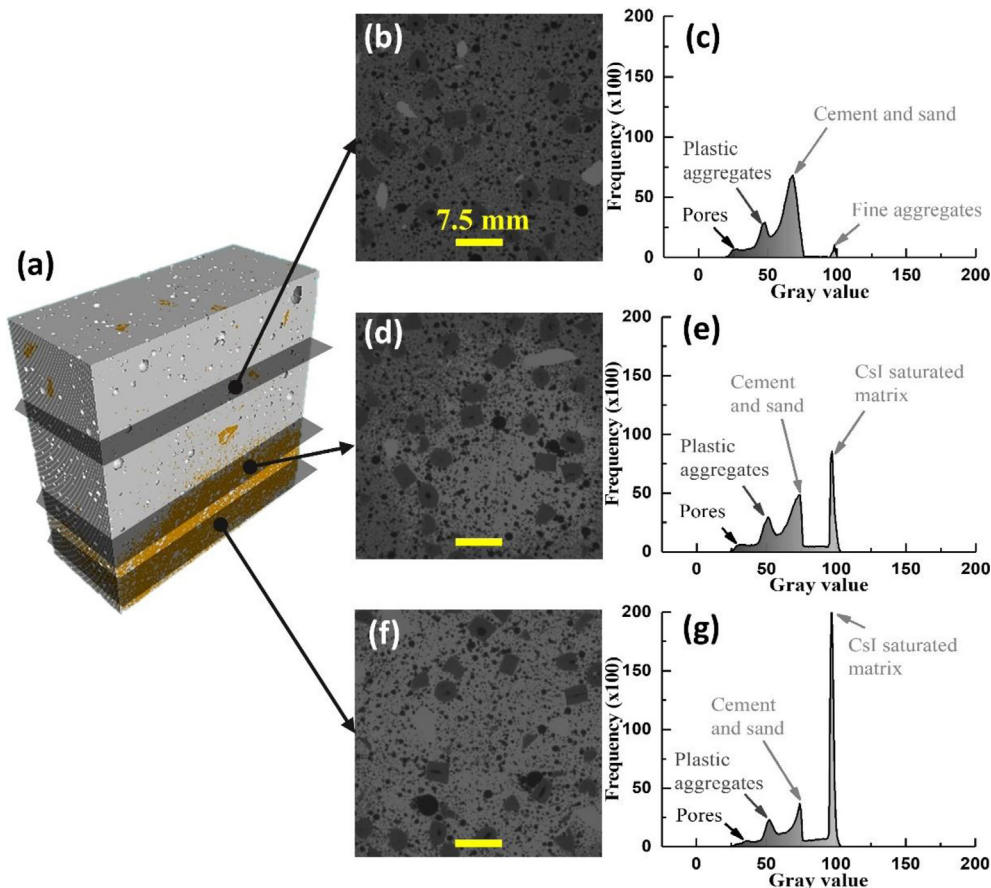
Fig. 10. An example of the μ-XCT analyses to evaluate water sorption of P10E2 for 360 min: (a) 3D demonstration of the cement matrix (gray) and the penetrated CsI solution (orange), (b) 2D sectional image near top surface showing no sign of CsI solution and the gray value distribution (c), (d) 2D sectional image showing partial CsI penetration and the gray value distribution (e), and (f) 2D sectional image near bottom surface showing full CsI penetration and the gray value distribution (g). (For interpretation of the references to colour in this figure legend, the reader is referred to the web version of this article.)

The gap between specimens with EVA and Ref and P10 increased again as more water particles continued to penetrate filling more isolated and connected pores. After being immersed for 540 min, the penetrations in Ref and P10 specimens were around 52 %, while other polymer-modified cementitious composites barely reached 33 %. These results were in good agreement with those calculated for mass sorptivity presented in Fig. 9b and c.

3.4. SEM/EDS analyses

The incorporation of organic and inorganic additives in cementitious composites can significantly impact their physical and chemical characteristics [29,126]. Fig. 13 selectively shows SEM images of the specimens at different magnifications. In the images, different phases, i.e., calcium–silicate–hydrate (CSH), ettringite (AFt), calcium hydroxide (CH), EVA, plastic aggregates, and the aggregate-matrix interfaces were marked. For the Ref sample, cement hydration products, such as CSH, CH and AFt, filled inter-particle gaps, generating relatively dense microstructure (Fig. 13a). For the mixture with 10 % RWP aggregate (P10), relatively coarse cement matrix was observed, and short fibrous AFt crystals were found in cavities and/or pores of the sample (Fig. 13b). Local sites of the higher magnification images of Fig. 13a and b verify the presence of regular hydration products in the mortar skeletons. However, the ITZ between the cement matrix and the plastic particle in P10 witnessed higher growth of fibrous AFt crystals that may account of weaker bond between these two components [21]. The more porous cement matrix of
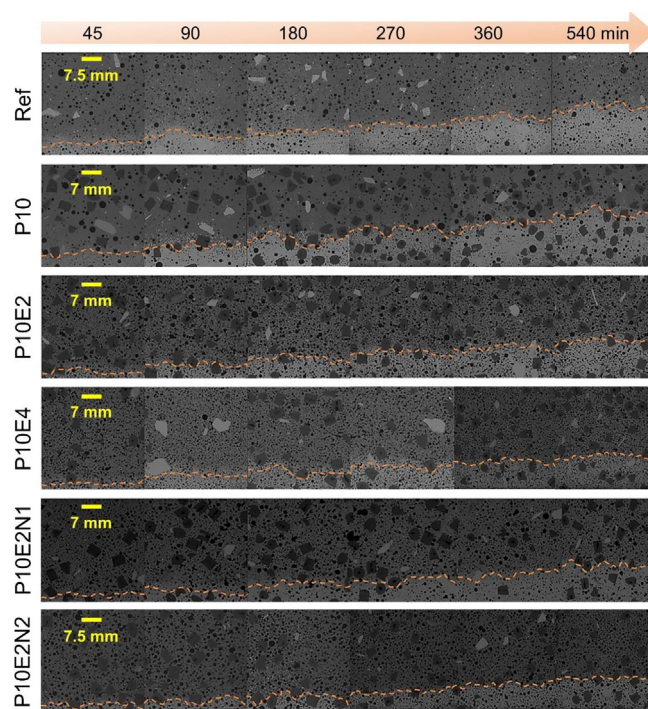
Fig. 11. μ-XCT profiles of the specimens showing CsI invasion over time: Rows 1 to 6 show the cementitious composites in order of Ref, P10, P10E2, P10E4, P10E2N1, and P10E2N2. Columns 1 to 6 represent time evolution in order of 45, 90, 180, 270, 360, and 540 min.

the P10 sample than that of the Ref sample may account for its lower strength (Figs. 5 and 6).

Changes in the micro morphologies were clear in the EVA-modified composites (Fig. 13c and d). EVA reacted with water and created interconnected polymer films that altered the nucleation and growth of typical cement hydration products (CSH, CH, and AFt). For instance, AFt needles together with EVA copolymer, formed a mixture that can fill the interparticle gaps (Fig. 13c). In the P10E4 sample, EVA agglomerated together to generate polymer films (Fig. 13d), and shrinkage of the EVA films may induce an interconnected foam-like structure [127] (see also Fig. 3). The existence of EVA films around the plastic particles (as shown in the higher magnification images of P10E2 and P10E4) shows that these films can partially coat aggregates and to some extent fill the pores in the ITZs [128]. These films can naturally obstruct the path for water transport, which greatly develop better waterproofing performance when EVA was mixed in the mixtures (Figs. 9 and 12).

Furthermore, it has been reported that EVA retards cement hydration due to the partial enclosure of cement grains [129] and consumption of intermolecular bonds due to the reaction between EVA and CH [29,117]. The addition of nS into the mixtures generated more CSH gel and longer AFt needles (Fig. 13e and f), probably owing to the effects of filling and heterogeneous nucleation that can accelerate cement hydration.

BSE/EDS tests were conducted to trace CsI at different locations of the specimens (Fig. 14). Here, the results collectively testified that the contrast enhancement for XCT can be expanded to other microscopic techniques based on X-ray scans. As an example, Fig. 14a represents a vertical cross-section of the P10E2N1 specimen after being immersed in CsI solution for 360 min. Three regions of interest (ROI) were selected for further EDS scans (Fig. 14a): a) ROI-I in the area without liquid penetration, b) ROI-II on the liquid penetration front, and c) ROI-III in the area fully penetrated with the CsI solution. EDS line and map scans were per-
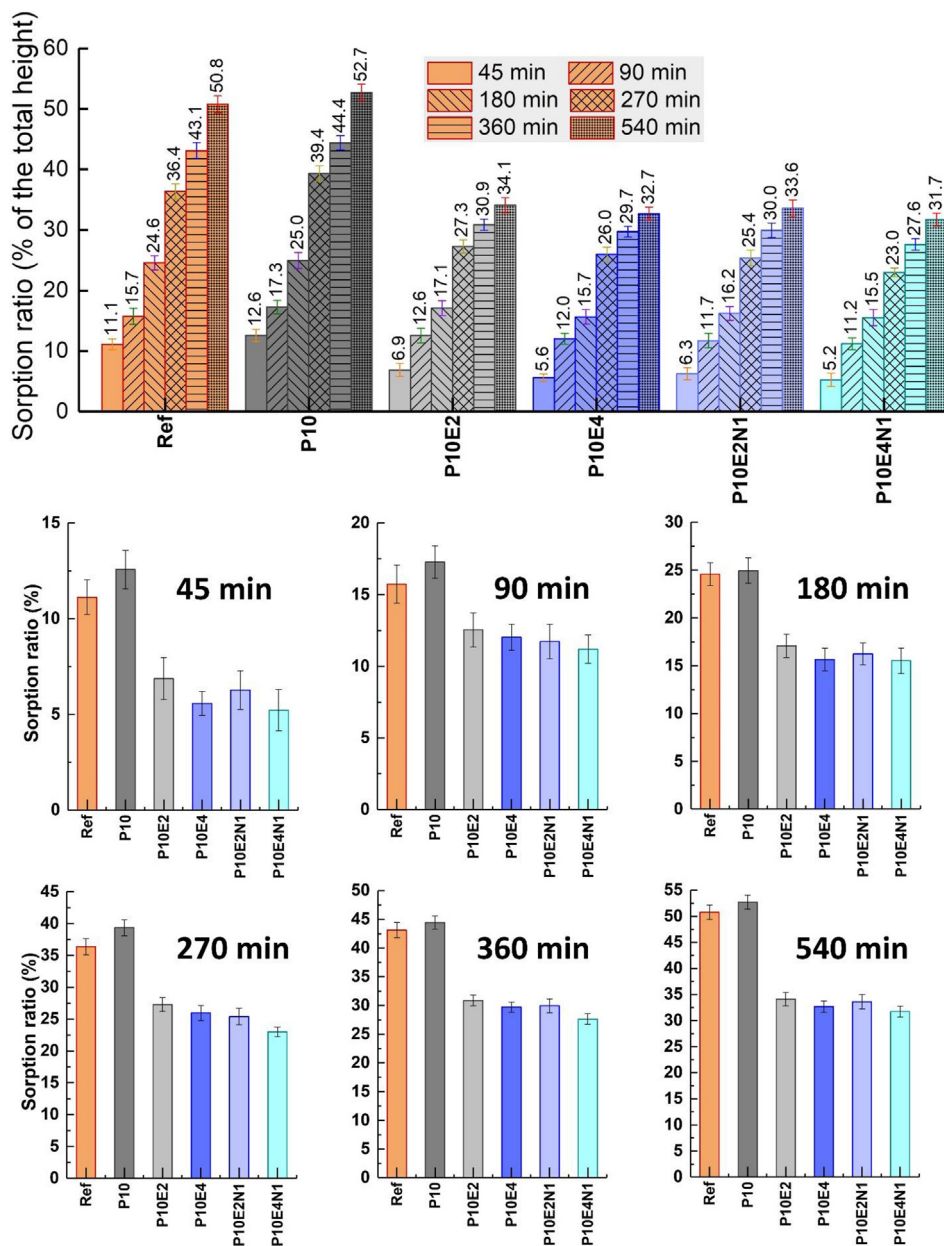

Fig. 12. Penetration rate of specimens as a ratio of the total height after being immersed in CsI solution for 45, 90, 180, 270, 360, and 540 min.
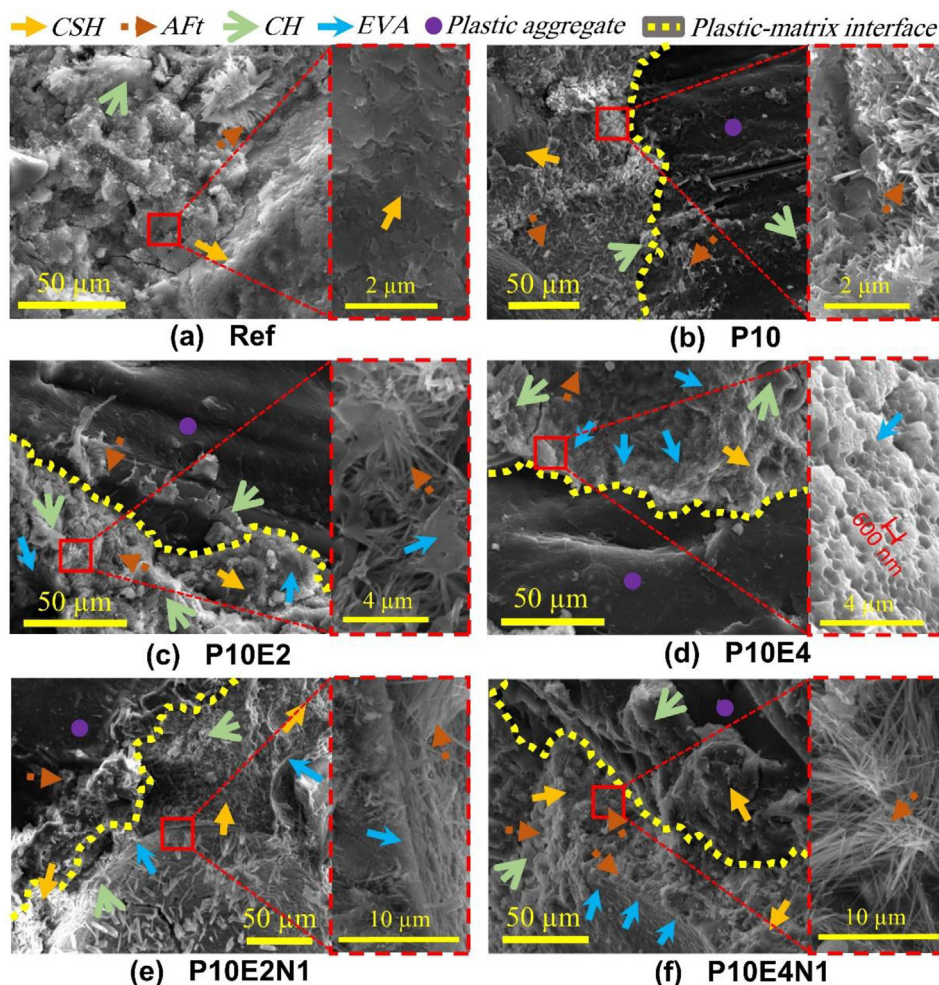
Fig. 13. SEM images of cementitious composites: (a) Ref, (b) P10, (c) P10E2, (d) P10E4, (e) P10E2N1, and (f) P10E4N1.

formed to monitor the chemical distributions in the selected ROIs. Calcium (Ca), oxygen (O), silicon (Si), carbon (C), cesium (Cs), and iodide (I) were specifically detected. Analyses showed that Ca and O appeared as expected in the cement matrix and sand grains; Si dominated over sand particles, but was observed in the cement matrix due to the addition of nS; C showed up primarily over plastic, yet it was detected in the cement matrix owing to the use of EVA in this mixture (Fig. 14b, c, and d).
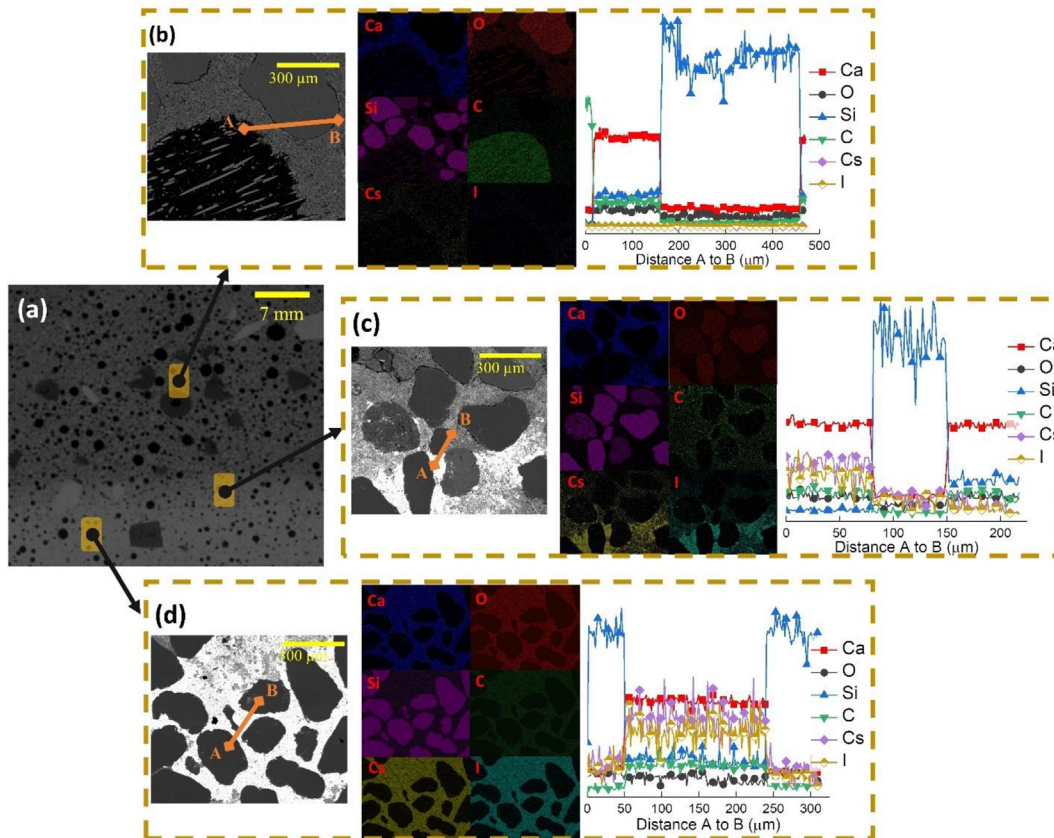
For the ROI-II on the CsI solution penetration front, white blotches that represent the CsI penetrated part of the cement matrix were observed, because the BSE signals are also proportions to the density of a phase or the atomic number of an element [83]. Cs and I were clearly detected in the mapping analyses as shown in Fig. 14c, due to their high atomic numbers. In the line scan, because the line started at a penetrated location (A), high intensities of Cs and I were recorded. Also, the white blotches were more likely to appear around sand grains, indicating that the CsI solution tended to penetrate through the weak aggregates-matrix interface. Similarly, Fig. 14d shows the results of ROI-III at a fully penetrated area. More white blotches all over the image were observed, verifying the full penetration of the CsI solution. Element mapping scans and line analysis evidently showed the filling of Cs and I in the porous cement matrix. On a side note, this indicated that heavy elements may also facilitate to build highly contrast images for BSE and EDS tests [83]. Extensive applications can be envisaged for the detection of porous phases for liquid penetration.

4. Mechanism and further discussion

The experimental results explicitly imply that not only waste plastics could be recycled seamlessly in CBMs, but they can also show enhanced durability in terms of pseudo-ductility and waterproofing performance. Strength reductions may be a common problem when reusing waste materials, while the implications and long—term uses of materials with enhanced integrative properties are diversified in the practical engineering field [1,130], especially when cost of raw natural materials is a cause of concern. The continuous improvements within more interconnected research fields (e.g. materials, environment, physics, etc.) would lessen the accompanying shortcomings of recycled materials and finally achieve equivalent properties of that of natural raw materials.

Fig. 15 shows a schematic illustration of RWP cementitious composites with and without the hybrid effect of EVA-nS, which demonstrates the tunned microstructure and liquid transport. EVA that generated interconnected films and nS particles that functioned as nanofillers jointly obstruct the channels for water migration. Hydration starts as cement is mixed with water, where mainly CSH, CH, and AFt grow in undefined shapes filling most of the pore spaces that were initially filled with water (Fig. 13). The remaining unfilled micro- and nano-scale pores function as isolated and connected paths for liquid migration [33].

When liquid transforms through a typical cement matrix (Fig. 15a1), the inter-particle spaces provide penetration paths

Fig. 14. BSE images and EDS analysis of the P10E2N1 sample at different locations after being immersed in CsI solution for 360 min: (a) ROIs of EDS analysis, (b) EDS results of ROI-I at the upper part of the specimen, (c) EDS results of ROI-II on the penetration fronts, and (d) EDS results of ROI-III at the bottom part with full CsI penetration.

allowing for higher penetration fronts as probed by μ-XCT in Fig. 11 (see the schematic illustration in Fig. 15a2). In contrary, cementitious composites modified with EVA and nS have substan-

tial high waterproofing performance. The mechanisms work when EVA is firstly mixed with water and other components. On one hand, EVA polymers entrain more voids in the cement matrix [33,88], and seal the channels for water migration. On the other hand, nS particles fill more spaces in the cement matrix, which results in densified microstructure that enables more EVA-film connections (Fig. 3). Here, the hybrid effect of this composite structure block mass migration (Fig. 15b2) while maintaining high porosity (Fig. 7).
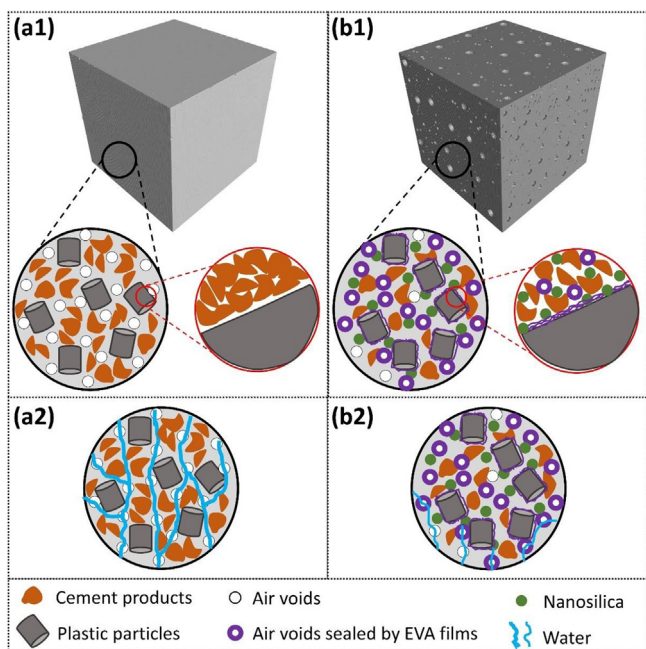
Fig. 15. Schematic illustration: (a1) RWP cementitious composite with its components and water penetration paths (a2); (b1) EVA-nS modified RWP cementitious composite with its components and mechanism of blocking water penetration paths by the hybrid effect of EVA films and nanosilica particles (b2).
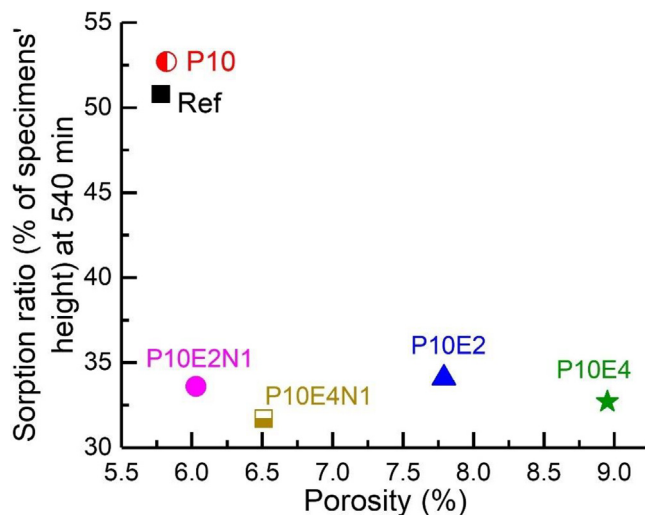
Fig. 16. Relationship between porosity and sorption ratio of the 540-min water uptake for all specimens.

To further explicate the waterproofing performance of typical and polymer-modified specimens, P10 and P10E4 are compared with some details. In addition to EVA in P10E4, both composites consist of cement, sand, RWPs, and water. Based on the porosity values and sorption ratios (or sorption heights) for 540 min of specimens (Figs. 7 and 12), significant waterproof effect of EVA and nS is testified in Fig. 16. For P10, this resulted in ~6 % porosity and ~53 % sorption height in 540 min as probed by μ-XCT (Figs. 7 and 11). As for P10E4, however, the effect of EVA emulsion can be seen at the hydration process, where various air voids are entrapped within the hydrated composites because EVA particles partially wrapped cement particles and somewhat deprived them from hydration [93], which resulted in cement-based composite with higher porosity. At the same time, EVA emulsion created polymer films (as observed in Fig. 3) that to some extent sealed the connected channels in the porous system of the P10E4 matrix resulting in blocking liquid migration paths [33,127]. In other words, waterproofing performance was substantially enhanced allowing for ~32 % of the total height to be penetrated in 540 min while the porosity was ~9 %. It is worth noting that nS particles worked as nanofillers in P10E2N1 and P10E4N1 and decreased the porosity, which was beneficial for strengths, while keeping excellent waterproofing performance.

To understand the difference and affecting parameters between mass sorptivity (S_m) and depth sorptivity (S_l), their results were correlated using Eq. (5), assuming homogenous pore structures of specimens. From the penetration heights in Fig. 12 based on μ-XCT images in Fig. 11, S_l was calculated using Eq. (3). Fig. 17 shows the correlation between S_m and S_l. As expected, positive correlations between both characteristics (S_m and S_l) were observed in all specimens. Obviously from the slope values, the six different mixtures could be categorized in three main groups: Ref&P10, P10E2&P10E4, and P10E2N1&P10E4N1, which could also be noted from the changes occurred to the porosity between specimens (see Fig. 7). Given the ability of polymers and nS to improve waterproofing performance [94,131] and alter microstructures, one can notice that at any value of mass sorptivity, say 0.02 g/s^0.5, the depth sorptivity can vary remarkably, where it could be at an average of 0.077 mm/s^0.5 for P10E2&P10E4 and 0.11 mm/s^0.5 for Ref&P10. This shows how noteworthy the alterations to the microstructures of polymer-modified cementitious composites are even at small quantities compared with typical specimens. These observations, therefore, shed more light on how related parameters could affect waterproofing performance directly or inversely.
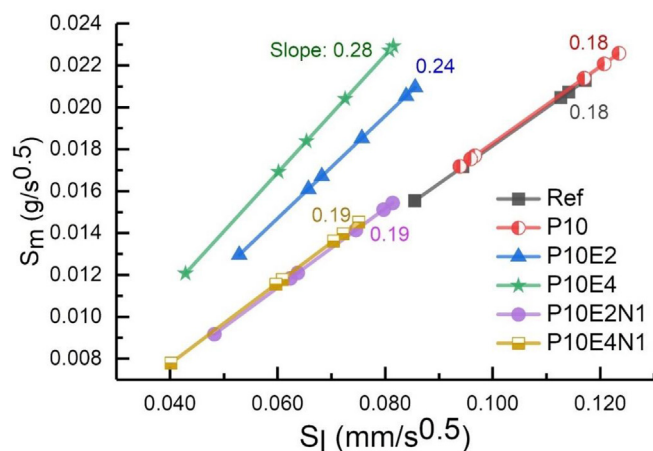
5. Concluding remarks

In this work, recyclability of RWP in cementitious materials was enhanced by using 2–4 % EVA and 1 % nS that led to better compatibility between the plastic aggregates and the cement matrix. In particular, waterproof performance of the EVA-nS-engineered RWP cementitious composites was thoroughly assessed by a non-destructive μ-XCT test with the contrast enhancing agent of CsI. In addition, the microstructure of the cementitious composites was tested by comprehensive techniques (SEM/BSE and EDS). The following concluding remarks of this research can be drawn:

- The EVA-nS hybrids enabled recyclability enhancement of RWPs in cementitious composites showing improved pseudo-ductility and mitigated strength reductions (~4% and over 2 % in compressive and flexural strengths, respectively).
- The polymerized EVA particles can greatly affect the microstructure of cementitious composites resulting in higher porosities. In contrast, 25 % reduction in porosities was observed when nS was implemented in the mixtures owing to the nanofilling effect.
- Significant improvements in waterproof performance were detected for the EVA-nS hybrid cementitious composites. Average sorptivity reductions by over 50 % were recorded. The effect of nS on the sorptivity reductions was not significant compared with EVA.
- EVA formed polymers in cement matrix, affecting the main cement hydration products (i.e. CSH, CH, and AFt). The polymeric EVA films obstructed the connected channels in the specimens, which resulted in significantly higher waterproofing performance.

In addition to mitigating strengths of RWP cementitious composites by EVA-nS hybrids, this work affirms substantial improvement of waterproofing performance of RWP cementitious composites. Moreover, specific transport mechanisms and engineering parameters are yet to be extensively elaborated in future work taking advantage of contrast-enhancement agents (e.g. CsI) and the accessibility to μ-XCT, SEM/BSE, and EDS techniques. Going beyond this, the findings would pave a path toward design and fabrication of organic–inorganic composites for large scale engineering applications.

CRediT authorship contribution statement

Ahmed Al-Mansour: Methodology, Software, Data curation, Writing – original draft. **Rijiao Yang:** Methodology, Software, Data curation. **Chengji Xu:** Methodology, Software, Data curation. **Yuqing Dai:** Software, Data curation. **Yu Peng:** Methodology, Software, Supervision. **Jiyang Wang:** Conceptualization, Supervision. **Qing Lv:** Conceptualization, Supervision. **Le Li:** Software, Writing – review & editing. **Chunsheng Zhou:** Writing – review & editing, Supervision. **Zhidong Zhang:** Writing – review & editing, Supervision. **Qiang Zeng:** Conceptualization, Writing – review & editing, Supervision. **Shilang Xu:** Writing – review & editing, Supervision.

Data availability

The raw/processed data that support the findings of this study are available upon reasonable request.

Declaration of Competing Interest

The authors declare that they have no known competing financial interests or personal relationships that could have appeared to influence the work reported in this paper.

Fig. 17. Correlation between mass sorptivity (S_m) from Eq. (5) and depth sorptivity (S_l) from Eq. (3) with penetration height calculated in Fig. 12 from μ-XCT images.

Acknowledgements

References

[1] S. Gupta, S. Chaudhary, State of the art review on supplementary cementitious materials in India – II: characteristics of SCMs, effect on concrete and environmental impact, J. Clean. Prod. 357 (2022) 131945.

[2] UNEP, The Global Alliance for Buildings and Construction: An Overview Over Status and Achievements, 2022.

[3] S.M.S. Kazmi, M.J. Munir, Y.-F. Wu, Application of waste tire rubber and recycled aggregates in concrete products: a new compression casting approach, Resour. Conserv. Recycl. 167 (2021) 105353.

[4] P.O. Awoyera, E.I. Ugwu, 19 - Overview on environmental impact of recycled aggregate concrete incorporating pozzolans or fillers, in: P.O. Awoyera, C. Thomas, M.S. Kirgiz (Eds.), The Structural Integrity of Recycled Aggregate Concrete Produced With Fillers and Pozzolans, Woodhead Publishing, 2022, pp. 435–444.

[5] Colangelo, F., Handbook of Sustainable Concrete and Industrial Waste Management, in: R.C. Francesco Colangelo, I. Farina (Eds.), Recycled and Artificial Aggregate, Innovative Eco-friendly Binders, and Life Cycle Assessment, Vol. 1, Elsevier, 2021.

[6] R. Kumar et al., Impacts of plastic pollution on ecosystem services, sustainable development goals, and need to focus on circular economy and policy interventions, Sustainability 13 (17) (2021) 9963.

[7] S.I. Basha et al., Durability of recycled waste plastic aggregate concrete, Eur. J. Environ. Civ. Eng. (2022) 1–22.

[8] Y. Leow et al., A tough, biodegradable and water-resistant plastic alternative from coconut husk, Compos. B Eng. 241 (2022) 110031.

[9] Material Economics, The Circular Economy - a Powerful Force for Climate Mitigation, Sweden, 2018.

[10] J.R. Correia, J.S. Lima, J. de Brito, Post-fire mechanical performance of concrete made with selected plastic waste aggregates, Cem. Concr. Compos. 53 (2014) 187–199.

[11] A. Behnood, M. Ghandehari, Comparison of compressive and splitting tensile strength of high-strength concrete with and without polypropylene fibers heated to high temperatures, Fire Saf. J. 44 (8) (2009) 1015–1022.

[12] C. Albano et al., Influence of content and particle size of waste pet bottles on concrete behavior at different w/c ratios, Waste Manage. 29 (10) (2009) 2707–2716.

[13] S. Akçaözoğlu, he effect of elevated temperature on the lightweight concrete containing waste PET aggregate, Int. J. Bus. Technol. 6 (3) (2018).

[14] A. Cabanes, F.J. Valdés, A. Fullana, A review on VOCs from recycled plastics, Sustainable Mater. Technol. 25 (2020) e00179.

[15] N. Saikia, J. de Brito, Use of plastic waste as aggregate in cement mortar and concrete preparation: a review, Constr. Build. Mater. 34 (2012) 385–401.

[16] F.V.W. Appels et al., Fabrication factors influencing mechanical, moisture- and water-related properties of mycelium-based composites, Mater. Des. 161 (2019) 64–71.

[17] H.M. Adnan, A.O. Dawood, Recycling of plastic box waste in the concrete mixture as a percentage of fine aggregate, Constr. Build. Mater. 284 (2021) 122666.

[18] A. Al-Mansour et al., Green concrete: by-products utilization and advanced approaches, Sustainability 11 (19) (2019) 5145.

[19] S.N. Shah et al., Lightweight foamed concrete as a promising avenue for incorporating waste materials: a review, Resour. Conserv. Recycl. 164 (2021) 105103.

[20] A. Aattache, Properties and durability of partially replaced cement-based composite mortars co-using powders of a nanosilica superplasticiser and finely ground plastic waste, J Build. Eng. 51 (2022) 104257.

[21] A. Al-Mansour et al., Sustainable cement mortar with recycled plastics enabled by the matrix-aggregate compatibility improvement, Constr. Build. Mater. 318 (2022) 125994.

[22] N. Dulsang et al., Characterization of an environment friendly lightweight concrete containing ethyl vinyl acetate waste, Mater. Des. 96 (2016) 350–356.

[23] J. Thorneycroft et al., Performance of structural concrete with recycled plastic waste as a partial replacement for sand, Constr. Build. Mater. 161 (2018) 63–69.

[24] R.H. Faraj, A.F.H. Sherwani, A. Daraei, Mechanical, fracture and durability properties of self-compacting high strength concrete containing recycled polypropylene plastic particles, J Build. Eng. 25 (2019) 100808.

[25] S.S. Ali et al., Degradation of conventional plastic wastes in the environment. A review on current status of knowledge and future perspectives of disposal, Sci. Total Environ. (2021) 144719.

[26] F.K. Alqahtani, I. Zafar, Plastic-based sustainable synthetic aggregate in Green Lightweight concrete – a review, Constr. Build. Mater. 292 (2021) 123321.

[27] R.K. Dhir, P.C. Hewlett, Y.N. Chan, Near surface characteristics of concrete: intrinsic permeability, Mag. Concr. Res. 41 (147) (1989) 87–97.

[28] H. Li et al., Influence of defoaming agents on mechanical performances and pore characteristics of Portland cement paste/mortar in presence of EVA dispersible powder, J Build. Eng. 41 (2021) 102780.

[29] G. Liang et al., Synergistic effect of EVA, TEA and C-S-Hs-PCE on the hydration process and mechanical properties of Portland cement paste at early age, Constr. Build. Mater. 272 (2021) 121891.

[30] N.M. Sigvardsen, M.R. Geiker, L.M. Ottosen, Reaction mechanisms of wood ash for use as a partial cement replacement, Constr. Build. Mater. 286 (2021) 122889.

[31] N.M. Sigvardsen, M.R. Geiker, L.M. Ottosen, Phase development and mechanical response of low-level cement replacements with wood ash and washed wood ash, Constr. Build. Mater. 269 (2021) 121234.

[32] Z. Shi et al., Synthesis of alkali-silica reaction product structurally identical to that formed in field concrete, Mater. Des. 190 (2020) 108562.

[33] Y. Peng et al., In-situ assessment of the water-penetration resistance of polymer modified cement mortars by μ-XCT, SEM and EDS, Cem. Concr. Compos. 114 (2020) 103821.

[34] M. Nofar, R. Salehiyan, S.S. Ray, Influence of nanoparticles and their selective localization on the structure and properties of polylactide-based blend nanocomposites, Compos. B Eng. 215 (2021) 108845.

[35] C. Nunes et al., Microstructure of lime and lime-pozzolana pastes with nanosilica, Cem. Concr. Res. 83 (2016) 152–163.

[36] B. Cantero et al., Water transport and shrinkage in concrete made with ground recycled concrete-additioned cement and mixed recycled aggregate, Cem. Concr. Compos. 118 (2021) 103957.

[37] C. Hall, Capillary imbibition in cement-based materials with time-dependent permeability, Cem. Concr. Res. 124 (2019) 105835.

[38] F. Ren et al., Quantifying the anomalous water absorption behavior of cement mortar in view of its physical sensitivity to water, Cem. Concr. Res. 143 (2021) 106395.

[39] C. Hall, Water movement in porous building materials—I. Unsaturated flow theory and its applications, Build. Environ. 12 (2) (1977) 117–125.

[40] B. Aïssoun, K. Khayat, J.L. Gallias, Variations of sorptivity with rheological properties of concrete cover in self-consolidating concrete, Constr. Build. Mater. 113 (2016) 113–120.

[41] C. Hall, Water sorptivity of mortars and concretes: a review, Mag. Concr. Res. 41 (147) (1989) 51–61.

[42] D. Vafaei et al., Sorptivity and mechanical properties of fiber-reinforced concrete made with seawater and dredged sea-sand, Constr. Build. Mater. 270 (2021) 121436.

[43] S. Kelham, A water absorption test for concrete, Mag. Concr. Res. 40 (143) (1988) 106–110.

[44] ASTM C1585/C1585M-13, Standard Test Method for Measurement of Rate of Absorption of Water by Hydraulic-Cement Concretes, ASTM International, West Conshohocken, PA, 2013, www.astm.com.

[45] BS, E.N., Steel Tubes and Fittings for Onshore and Offshore Pipelines - External Liquid Applied Polyurethane and Polyurethane-modified Coatings, 2002, p. 1–48.

[46] N.S. Martys, C.F. Ferraris, Capillary transport in mortars and concrete, Cem. Concr. Res. 27 (5) (1997) 747–760.

[47] H. Baji et al., Analytical models for effective hydraulic sorptivity, diffusivity and conductivity of concrete with interfacial transition zone, Constr. Build. Mater. 225 (2019) 555–568.

[48] L. Hanžič, R. Ilić, Relationship between liquid sorptivity and capillarity in concrete, Cem. Concr. Res. 33 (9) (2003) 1385–1388.

[49] W. Kubissa, R. Jaskulski, M. Grzelak, Torrent air permeability and sorptivity of concrete made with the use of air entraining and citric acid as setting retardant, Constr. Build. Mater. 268 (2021) 121703.

[50] B.M. Aïssoun, J.L. Gallias, K.H. Khayat, Influence of formwork material on transport properties of self-consolidating concrete near formed surfaces, Constr. Build. Mater. 146 (2017) 329–337.

[51] L. Chen et al., Mechanical property, sorptivity and microstructure of steam-cured concrete incorporated with the combination of metakaolin-limestone, Case Stud. Constr. Mater. 11 (2019) e00267.

[52] L.G. Li et al., Synergistic cementing efficiencies of nano-silica and micro-silica in carbonation resistance and sorptivity of concrete, J Build. Eng. 33 (2021) 101862.

[53] R. Liu et al., Improving the microstructure of ITZ and reducing the permeability of concrete with various water/cement ratios using nano-silica, J. Mater. Sci. 54 (1) (2019) 444–456.

[54] R. Choudhary et al., Sorptivity characteristics of high strength self-consolidating concrete produced by marble waste powder, fly ash, and micro silica, Mater. Today:. Proc. 32 (2020) 531–535.

[55] M.M. Hossain et al., Water absorption and sorptivity of alkali-activated ternary blended composite binder, J Build. Eng. 31 (2020) 101370.

[56] K. Yang et al., Establishment of a preconditioning regime for air permeability and sorptivity of alkali-activated slag concrete, Cem. Concr. Compos. 73 (2016) 19–28.

[57] S. Ruan et al., Waterproof geopolymer composites modified by hydrophobic particles and polydimethylsiloxane, Compos. B Eng. 237 (2022) 109865.

[58] J.L. Lage, THE fundamental theory of flow through permeable media from Darcy to turbulence†, †Dedicated in memory of my dear friend and father-in-law, Mr. Fernando D'olne Soares de Barros, 1902–1997, in Transport Phenomena in Porous Media, D.B. Ingham and I. Pop, Editors, Pergamon, Oxford, 1998, pp. 1–30.

[59] L.A. Richards, Capillary conduction of liquids through porous mediums, Physics 1 (5) (1931) 318–333.

[60] S. Tsivilis et al., The permeability of Portland limestone cement concrete, Cem. Concr. Res. 33 (9) (2003) 1465–1471.

[61] Q. Zeng et al., Reassessment of mercury intrusion porosimetry for characterizing the pore structure of cement-based porous materials by monitoring the mercury entrapments with X-ray computed tomography, Cem. Concr. Compos. 113 (2020) 103726.

[62] R. Qian et al., Radial gas-permeability measurement in cement-based materials under steady-state flow, Flow Meas. Instrum. 79 (2021) 101896.

[63] Y. Mualem, A new model for predicting the hydraulic conductivity of unsaturated porous media, Water Resour. Res. 12 (3) (1976) 513–522.

[64] C. Zhou et al., Indirect assessment of hydraulic diffusivity and permeability for unsaturated cement-based material from sorptivity, Cem. Concr. Res. 82 (2016) 117–129.

[65] E. Xie et al., The effect of chemical aging on water permeability of white cement mortars in the context of sol–gel science, Cem. Concr. Compos. 114 (2020) 103812.

[66] W. Wang et al., Investigation of water ingress into uncracked and cracked cement-based materials using electrical capacitance volume tomography, Mater. Des. (2022) 110877.

[67] J. Cid, J.F. Alquier, P. Crausse, Study of moisture transfer in a deformable porous medium through attenuation of two different energy gamma rays, Rev. Sci. Instrum. 63 (3) (1992) 2057–2064.

[68] H.S. Isfahani et al., Investigation on gamma-ray shielding and permeability of clay-steel slag mixture, Bull. Eng. Geol. Environ. 78 (6) (2019) 4589–4598.

[69] P.J. McGlinn et al., Appraisal of a cementitious material for waste disposal: neutron imaging studies of pore structure and sorptivity, Cem. Concr. Res. 40 (8) (2010) 1320–1326.

[70] P.J. McDonald et al., Sorption, anomalous water transport and dynamic porosity in cement paste: a spatially localised 1H NMR relaxation study and a proposed mechanism, Cem. Concr. Res. 133 (2020) 106045.

[71] T. Oesch et al., Correction to: quantitative in-situ analysis of water transport in concrete completed using X-ray computed tomography, Transport Porous Media **127**(2) (2019) 391.

[72] P. Zhang et al., Neutron radiography, a powerful method to determine time-dependent moisture distributions in concrete, Nucl. Eng. Des. 241 (12) (2011) 4758–4766.

[73] P. Zhang et al., Application of neutron imaging to investigate fundamental aspects of durability of cement-based materials: a review, Cem. Concr. Res. 108 (2018) 152–166.

[74] K. Xu et al., Microstructure and water absorption of ancient concrete from Pompeii: an integrated synchrotron microtomography and neutron radiography characterization, Cem. Concr. Res. 139 (2021) 106282.

[75] Z. Fisher et al., Chapter 1 - biological structures, in: F. Fernandez-Alonso, D.L. Price (Eds.), Experimental Methods in the Physical Sciences, Academic Press, 2017, pp. 1–75.

[76] A. du Plessis, I. Yadroitsava, I. Yadroitsev, Effects of defects on mechanical properties in metal additive manufacturing: a review focusing on X-ray tomography insights, Mater. Des. 187 (2020) 108385.

[77] M.A. Boone et al., 3D mapping of water in oolithic limestone at atmospheric and vacuum saturation using X-ray micro-CT differential imaging, Mater. Charact. 97 (2014) 150–160.

[78] L. Yang et al., In-situ tracking of water transport in cement paste using X-ray computed tomography combined with CsCl enhancing, Mater. Lett. 160 (2015) 381–383.

[79] Y. Kawabata et al., In situ observation for the influence of hydraulic pressure on internal damage of cement-based materials, Mater. Des. 216 (2022) 110556.

[80] B. Masschaele et al., High-speed thermal neutron tomography for the visualization of water repellents, consolidants and water uptake in sand and lime stones, Radiat. Phys. Chem. 71 (3) (2004) 807–808.

[81] C. Willson, N. Lu, W. Likos, Quantification of grain, pore, and fluid microstructure of unsaturated sand from X-ray computed tomography images, Geotech. Test. J. 35 (6) (2012) 911–923.

[82] Q. Zeng et al., Capillary imbibition of ethanol in cement paste traced by X-ray computed tomography with CsCl-enhancing technique, Chem. Phys. Lett. 726 (2019) 117–123.

[83] Q. Zeng et al., Transmission micro-focus X-ray radiographic measurements towards in-situ tracing capillary imbibition fronts and paths in ultra-thin concrete slices, Measurement 175 (2021) 109141.

[84] M. Khanzadeh Moradllo, M.T. Ley, Quantitative measurement of the influence of degree of saturation on ion penetration in cement paste by using X-ray imaging, Constr. Build. Mater. 141 (2017) 113–129.

[85] M. Khanzadeh Moradllo, Q. Hu, M.T. Ley, Using X-ray imaging to investigate in-situ ion diffusion in cementitious materials, Constr. Build. Mater. 136 (2017) 88–98.

[86] S. Hong et al., Water distribution characteristics in cement paste with capillary absorption, Constr. Build. Mater. 240 (2020) 117767.

[87] Z. Ding et al., Water distribution characteristics and research with capillary absorption for magnesium phosphate cement-coated cement pastes, Constr. Build. Mater. 265 (2020) 120319.

[88] Y. Ohama, Polymer-based admixtures, Cem. Concr. Compos. 20 (2) (1998) 189–212.

[89] E. Sakai, J. Sugita, Composite mechanism of polymer modified cement, Cem. Concr. Res. 25 (1) (1995) 127–135.

[90] U. Sharma et al., Effect of particle size of nanosilica on microstructure of C-S-H and its impact on mechanical strength, Cem. Concr. Compos. 97 (2019) 312–321.

[91] M. Stefanidou, I. Papayianni, Influence of nano-SiO2 on the Portland cement pastes, Compos. B Eng. 43 (6) (2012) 2706–2710.

[92] H.M. Sujay et al., Experimental study on durability characteristics of composite fiber reinforced high-performance concrete incorporating nanosilica and ultra fine fly ash, Constr. Build. Mater. 262 (2020) 120738.

[93] D.A. Silva, P.J.M. Monteiro, Analysis of C3A hydration using soft X-rays transmission microscopy: effect of EVA copolymer, Cem. Concr. Res. 35 (10) (2005) 2026–2032.

[94] Y. Yang et al., Mechanical properties of EVA-modified cement for underground gas storage, J. Nat. Gas Sci. Eng. 27 (2015) 1846–1851.

[95] H. Du, S. Du, X. Liu, Effect of nano-silica on the mechanical and transport properties of lightweight concrete, Constr. Build. Mater. 82 (2015) 114–122.

[96] P. Sikora et al., Evaluating the effects of nanosilica on the material properties of lightweight and ultra-lightweight concrete using image-based approaches, Constr. Build. Mater. 264 (2020) 120241.

[97] A.M. Betioli et al., Effect of EVA on the fresh properties of cement paste, Cem. Concr. Compos. 34 (2) (2012) 255–260.

[98] P. Sikora et al., The effect of nanosilica on the mechanical properties of polymer-cement composites (PCC), Procedia Eng. 108 (2015) 139–145.

[99] G.H. Barbhuiya et al., Effects of the nanosilica addition on cement concrete: a review, Mater. Today: Proc. (2020).

[100] ASTM C143/C143M-20, Standard Test Method for Slump of Hydraulic-Cement Concrete, ASTM International, West Conshohocken, PA, 2020, www.astm.org.

[101] ASTM C78/C78M-18, Standard Test Method for Flexural Strength of Concrete (Using Simple Beam with Third-Point Loading), ASTM International, West Conshohocken, PA, 2018, www.astm.org.

[102] V. Baroghel-Bouny, Water vapour sorption experiments on hardened cementitious materials: Part I: essential tool for analysis of hygral behaviour and its relation to pore structure, Cem. Concr. Res. 37 (3) (2007) 414–437.

[103] H. Loosveldt, Z. Lafhaj, F. Skoczylas, Experimental study of gas and liquid permeability of a mortar, Cem. Concr. Res. 32 (9) (2002) 1357–1363.

[104] C. Li, Mechanical and transport properties of recycled aggregate concrete modified with limestone powder, Compos. B Eng. 197 (2020) 108189.

[105] M.K. Gopalan, Sorptivity of fly ash concretes, Cem. Concr. Res. 26 (8) (1996) 1189–1197.

[106] Z. Wu et al., Anomalous water absorption in cement-based materials caused by drying shrinkage induced microcracks, Cem. Concr. Res. 115 (2019) 90–104.

[107] L.J. Parrott, Moisture conditioning and transport properties of concrete test specimens, Mater. Struct. 27 (8) (1994) 460.

[108] Z. Wu, H.S. Wong, N.R. Buenfeld, Influence of drying-induced microcracking and related size effects on mass transport properties of concrete, Cem. Concr. Res. 68 (2015) 35–48.

[109] H.S. Wong et al., Effect of entrained air voids on the microstructure and mass transport properties of concrete, Cem. Concr. Res. 41 (10) (2011) 1067–1077.

[110] M.R. Geiker et al., Limit states for sustainable reinforced concrete structures, Cem. Concr. Res. 122 (2019) 189–195.

[111] R. Lucas, Ueber das Zeitgesetz des kapillaren Aufstiegs von Flüssigkeiten, Kolloid-Zeitschrift 23 (1) (1918) 15–22.

[112] J. Cai et al., Lucas-Washburn equation-based modeling of capillary-driven flow in porous systems, Langmuir 37 (5) (2021) 1623–1636.

[113] G. Czél, M.R. Wisnom, Demonstration of pseudo-ductility in high performance glass/epoxy composites by hybridisation with thin-ply carbon prepreg, Compos. A Appl. Sci. Manuf. 52 (2013) 23–30.

[114] R.-X. Yang et al., Influence of ultrasound on forming force in thin sheetmetal microforming using molten plastic as flexible punch, Mater. Des. 212 (2021) 110239.

[115] F. Ahmad, M.I. Qureshi, Z. Ahmad, Influence of nano graphite platelets on the behavior of concrete with E-waste plastic coarse aggregates, Constr. Build. Mater. 316 (2022) 125980.

[116] L. Li et al., Efficiencies of carbonation and nano silica treatment methods in enhancing the performance of recycled aggregate concrete, Constr. Build. Mater. 308 (2021) 125080.

[117] H. Li et al., Improvements in setting behavior and strengths of cement paste/mortar with EVA redispersible powder using C-S-Hs-PCE, Constr. Build. Mater. 262 (2020) 120097.

[118] S. Liu et al., Effects of thermal-cooling cycling curing on the mechanical properties of EVA-modified concrete, Constr. Build. Mater. 165 (2018) 443–450.

[119] G. Sang, Y. Zhu, G. Yang, Mechanical properties of high porosity cement-based foam materials modified by EVA, Constr. Build. Mater. 112 (2016) 648–653.

[120] Volume graphics, VGSTUDIO MAX, in Reference manual, Volume Graphics GmbH, 2020.

[121] F.B.P.d. Costa et al., Experimental study of some durability properties of ECC with a more environmentally sustainable rice husk ash and high tenacity polypropylene fibers, Constr. Build. Mater. 213 (2019) 505–513.

[122] R.P. Spragg et al., Wetting and drying of concrete using aqueous solutions containing deicing salts, Cem. Concr. Compos. 33 (5) (2011) 535–542.

[123] Z. Naseem et al., Antifoaming effect of graphene oxide nanosheets in polymer-modified cement composites for enhanced microstructure and mechanical performance, Cem. Concr. Res. 158 (2022) 106843.

[124] R.L. Blokhra, Y.P. Sehgal, Viscosity of cesium halides, rubidium nitrate, and rubidium Iodide in diethyleneglycol and aqueous diethyleneglycol at 25°C, J. Solution Chem. 5 (6) (1976) 399–403.

[125] D.A. Silva, P.J.M. Monteiro, Hydration evolution of C3S–EVA composites analyzed by soft X-ray microscopy, Cem. Concr. Res. 35 (2) (2005) 351–357.

[126] B. Yin et al., Performance cement-based composite obtained by in-situ growth of organic–inorganic frameworks during the cement hydration, Constr. Build. Mater. 336 (2022) 127533.

[127] A. Messan, P. Ienny, D. Nectoux, Free and restrained early-age shrinkage of mortar: Influence of glass fiber, cellulose ether and EVA (ethylene-vinyl acetate), Cem. Concr. Compos. 33 (3) (2011) 402–410.

[128] H.S. Wong et al., Influence of the interfacial transition zone and microcracking on the diffusivity, permeability and sorptivity of cement-based materials after drying, Mag. Concr. Res. 61 (8) (2009) 571–589.

[129] Y. Peng et al., BSE-IA reveals retardation mechanisms of polymer powders on cement hydration, J. Am. Ceram. Soc. 103(5) (2020) 3373–3389.

[130] I. Maruyama et al., Long-term use of modern Portland cement concrete: the impact of Al-tobermorite formation, Mater. Des. 198 (2021) 109297.

[131] P.S. Deb, P.K. Sarker, S. Barbhuiya, Sorptivity and acid resistance of ambient-cured geopolymer mortars containing nano-silica, Cem. Concr. Compos. 72 (2016) 235–245.